ACS OMEGA

http://pubs.acs.org/journal/acsodf

Article

Heterodinuclear Ru–Pt Complexes Bridged with 2,3-Bis(pyridyl)pyrazinyl Ligands: Studies on Kinetics, Deoxyribonucleic Acid/Bovine Serum Albumin Binding and Cleavage, In Vitro Cytotoxicity, and In Vivo Toxicity on Zebrafish Embryo Activities

Rajesh Bellam,* Deogratius Jaganyi, and Ross Stuart Robinson

Cite This: *ACS Omega* 2022, 7, 26226–26245

Read Online

ACCESS | Metrics & More | Article Recommendations | Supporting Information

ABSTRACT: Di- and poly-homo/heteronuclear complexes have great potential as anticancer drugs. Here, we report their reactivity, deoxyribonucleic acid (DNA)/bovine serum albumin (BSA) binding and cleavage interactions, in vitro cytotoxicity, and in vivo zebrafish embryo toxicity of $[(phen)_2Ru(\mu\text{-}L)PtCl_2]^{2+}$ (phen = 1,10-phenanthroline and *L* = 2,3-bis(2-pyridyl)pyrazine, bpp, $\mathbf{C_1}$; 2,3-bis(2-pyridyl)-quinoxaline, bpq, $\mathbf{C_{2ial}}$; 2,3-bis(2-pyridyl)benzo[*g*]quinoxaline, bbq, $\mathbf{C_3}$) anticancer prodrugs. The substitution reactivity increases from $\mathbf{C_1}$ to $\mathbf{C_3}$ owing to an increase in the π-conjugation on the bridging chelate which facilitates π-back bonding. As a result, the electrophilicity index on the $\mathbf{C_3}$ complex increases than that on the complex $\mathbf{C_2}$ followed by $\mathbf{C_1}$ which leads to higher rates of substitution and thus the reactivity order follows $\mathbf{C_1} < \mathbf{C_2} < \mathbf{C_3}$. The coordination of Ru at one end of each of the complexes enhances water solubility. Moreover, the charge addition of the two metal ions increases their reactivity toward substitution in addition to ensuring electrostatic interactions at target sites such as the DNA/BSA. Spectroscopic (UV–vis absorption and fluorescence quenching) titration and viscosity measurement results of the interactions of $\mathbf{C_{1/2/3}}$ with CT-DNA established the formation of stable, nonconvent $\mathbf{C_{1/2/3}}$-DNA adducts with DNA most likely via the intercalative binding mode. Furthermore, studies with BSA showed a good binding affinity of these complexes owing to hydrophobic interactions with the coordinated ligands. The interactions of these complexes with DNA/BSA are in line with the reactivity trend, and all these experimental findings were further supported by molecular docking analysis. In vitro MTT cytotoxic activities on human breast cancer cell line MCF-7 revealed that all the complexes have high cytotoxicity activity ($IC_{50} > 9$ μM); furthermore, the selectivity index and SI values were higher (>3). Complex $\mathbf{C_3}$ showed the highest cytotoxicity with $IC_{50} = 3.1$ μM and SI value (5.55) against MCF7 cell lines and these values were comparable to those of the cisplatin (IC_{50} and SI values are 5.0 μM and 4.02, respectively). In vivo toxicological assessments on zebrafish embryos revealed that all the Ru–Pt complexes ($\mathbf{C_{I/2/3}}$) have poor embryo acute toxic effects over 96 h postfertilization, hpf with $LC_{50} > 65.2$ μM. The complex $\mathbf{C_3}$ has shown the lowest embryo toxicity ($LC_{50} = 148.8$ μM), which is comparable to that of commercial cisplatin ($LC_{50} = 181.1$ μM). Based on the cytotoxicity results, complexes $\mathbf{C_2}$ and $\mathbf{C_3}$ could be considered for further development as chemotherapeutic agents against MCF breast cancer cells.

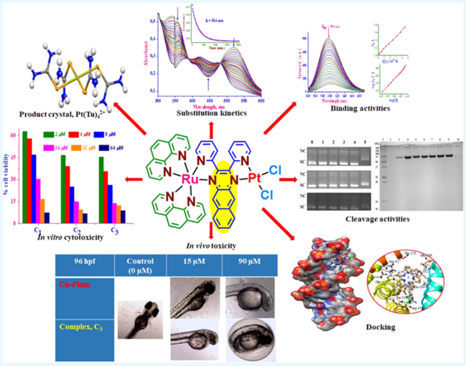

1. INTRODUCTION

The anticancer activity of mononuclear metallodrugs is attributed to their metal ions covalently binding to the N7 atoms of deoxyribonucleic acid's (DNA's) guanine/adenine bases as well as their noncovalent association via electrostatic, hydrogen bonding, and π–π stacking interactions (groove binding and intercalation) which also contribute to the stability of these adducts.[1−4] Researchers have explored and linked the interactions of metallodrugs with DNA to the antiproliferation of cancer cell lines, establishing DNA as the main site of action of the anticancer drugs. The interactions of metal complexes with DNA cause changes in DNA's molecular structure, including molecular cut-out effects, which eventually cause cancer cells to die. Data from studies that explore the reactivity trends of the interaction of metal complexes toward DNA or its N-donor biomimics or the competing S-nucleophiles are pivotal in the successful discovery of more effective anticancer metallodrugs. Furthermore, metallodrug–protein interactions are essential because the nature and strength of these noncovalent interactions have a great influence on drug absorption, distribution, metabolism, and excretion.[5] The

Received: March 30, 2022
Accepted: June 24, 2022
Published: July 21, 2022

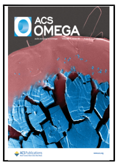

https://doi.org/10.1021/acsomega.2c01845
ACS Omega 2022, 7, 26226–26245

biodistribution of potential metal drugs can be modeled by studying their interactions with metal-ion carrier serum proteins such as serum albumins. Such metal complex–DNA/protein interactions are critical for the ultimate cytotoxicity of the metal drugs.

The most well-known and extensively researched metallodrugs are cisplatin, cis-$[Pt(NH_3)_2Cl_2]$[6] and its analogues. Platinum-based drugs have long been utilized as traditional chemotherapeutic drugs in the treatment of solid malignancies.[7] The serious negative side effects[8,9] and the incidence of drug resistance call for alternative and new types of metal-based anticancer drugs.[7,10,11] Ruthenium complexes have been reported as alternatives for platinum-based anticancer drugs. Ruthenium compounds have (i) reduced ligand exchange rates, allowing metal complexes to reach their biological targets unchanged, (ii) under physiological settings, they exist in a variety of stable oxidation states, and (iii) low nontarget toxicity due to their ability in binding to many biomolecules, such as serum transferrin and albumin.[12−14] NAMI/NAMI A, KP1019, NKP1339, and RAPTA-C, among other Ru(III) cationic anticancer drugs, are well-known for their antimetastatic properties and moderate-to-low cytotoxicity.[15−19] Furthermore, by varying the ancillary ligands, a vast platform of new Ru metallodrugs with tunable in vitro and in vivo properties can be synthesized.[20−22]

Dinuclear metal complexes (i) have more than one binding center, (ii) have increased water solubility owing to charge addition, and (iii) are likely to form stronger preassociative electrostatic interactions with DNA/bovine serum albumin (BSA) sequences compared to mononuclears. Incorporation of different metals into one molecule, that is, heterodinuclear metal complexes may induce better synergistic effects than the homodinuclear metal complexes. The metal atoms of heteronuclear complexes can be linked through a flexible aliphatic diamine/chain, rigid aromatic amines/molecules, or rigid bidentate or tridentate molecules. In this study, a series of heterodinuclear $[(phen)_2Ru(\mu\text{-}L)PtCl_2]^{2+}$ (phen = 1,10-phenanthroline and L = 2,3-bis(2-pyridyl)pyrazine), bpp, $\mathbf{C_1}$; 2,3-bis(2-pyridyl)quinoxaline, bpq, $\mathbf{C_2}$; 2,3-bis(2-pyridyl)-benzo[*g*]quinoxaline, bbq, $\mathbf{C_3}$) complexes were synthesized. The structures of the investigated Ru–Pt complexes are shown in Scheme 1. This was followed by studying their substitution kinetics and the interactions with DNA/BSA, as well as testing their in vitro cytotoxicity against selected human breast cancer cell line, MCF-7, and in vivo zebrafish embryos toxicities.

Scheme 1. Structural Formulas of Ru–Pt Heterobimetallic Complexes

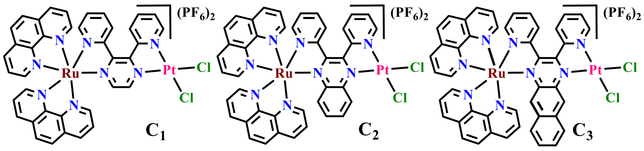

2. RESULTS AND DISCUSSION

2.1. Substitution Kinetics.

The substitution kinetics of chlorides from the Ru–Pt complexes by S-/N-donor nucleophiles (thiourea, Tu, L-methionine, L-Met, and guanosine-5′-monophosphate, 5′-GMP, structures are shown in Scheme 2) were investigated spectrophotometrically over the wavelengths ranging from 200 to 800 nm by following the change in absorbance as a function of time using a UV–vis spectrophotometer. A typical kinetic trace was recorded where there is a maximum build up or absorbance changes were noticed. The rate of the reaction was monitored at pH 7.2 (5 mM Tris–HCl/50 mM NaCl buffer) under pseudofirst-order conditions with respect to the Ru–Pt(II) complex, that is, concentrations of nucleophiles were prepared at least 20-fold in excess over that of the complex. The rates of the reactions were measured at 10 °C intervals at temperatures ranging from 25 to 55 °C. The concentration- and temperature-dependent rate constants, as well as the activation parameters, were calculated.

Scheme 2. Structural Formulas of Studied Nucleophiles

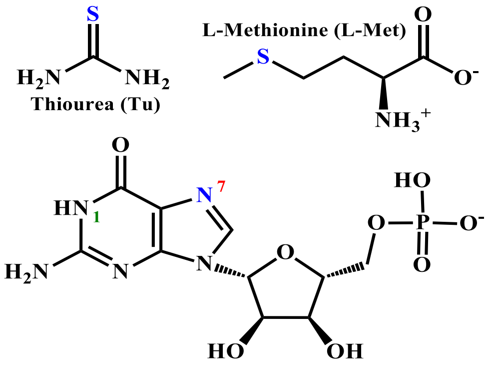

2.1.1. Reactions with Tu. Thiourea (Tu) is a very useful and widely used nucleophile in coordination chemistry for studying ligand substitution processes. The rate of reactions of Tu and the three Ru–Pt complexes was monitored spectroscopically. Representative Figure 1 depicts the spectral changes that occurred during the reaction of the complex $\mathbf{C_1}$ with Tu, with an inset depicting a typical kinetic trace of absorbance versus time at λ = 524 nm and T = 35 °C; also see ESI Figure S1 for the spectral changes of the complex $\mathbf{C_2}$ and $\mathbf{C_3}$ against Tu.

OriginPro 9.1 graphical analysis software was used to fit the absorbance versus time traces. All of the kinetic traces were

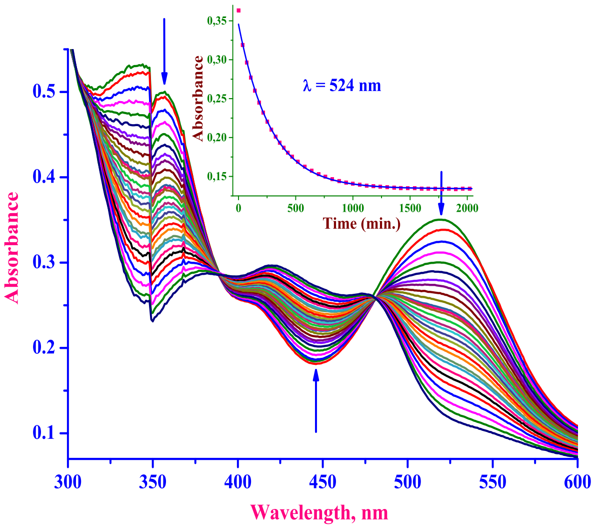

Figure 1. UV–vis spectral changes for the reaction between $\mathbf{C_1}$ (50 μM) and Tu (40-fold excess); the inset is a typical kinetic absorbance versus time trace at λ = 524 nm, pH = 7.2 (5 mM Tris–HCl/50 mM NaCl) and T = 35 °C.

found to be well fitted by nonlinear double-exponential functions, indicating that the reactions occurred in two substitution steps. The first step of each of the reactions is assigned to a substitution of the two chlorides simultaneously by Tu, which is relatively fast and exhibits linear concentration dependence with zero intercepts on the *y*-axis (see Figure 2a). This suggests a direct substitution according to the rate law:

$$k_{obs}{}^{1st} = k_2{}^{1st}\,[Nu] \tag{1}$$

where $k_2{}^{1st}$ is the second-order rate constant for the first step. The linear fit passing through the origin indicates that the rate of the possible parallel or backward reactions is minimum or nonexistent. The second step is slower and has a small intercept on the *y*-axis. This is either owing to the reverse reaction or a parallel slow back solvolysis of the double-substituted Tu intermediates of the complexes. This is followed by a rapid detachment of the bridging ligand from the Pt(II) metal center to form the Ru(2,3-bis(2-pyridyl)azine and $Pt(Tu)_4{}^{2+}$ as final products according to the rate law:

$$k_{obs}{}^{2nd} = k_2{}^{2nd}\,[Nu] + k_{-1}{}^{2nd} \tag{2}$$

where $k_2{}^{2nd}$ is the second-order rate constants for the formation of final product and $k_{-1}{}^{2nd}$ is the first-order rate constant associated with the back reaction despite the availability of excess chloride in solution to prevent the spontaneous hydrolysis of the complex. The release of a spectator ligand from the Pt(II) by Tu is probably owing to its strong *trans* effect as reported previously.[23] A simplified substitution reaction pathway is given in Scheme 3. The rates of reaction were studied as a function of temperature ranging from 25 to 55 °C at 10 °C intervals, the rate data at 35 °C are presented in Table 1, while the data for other temperatures are given in ESI Tables S1 and S2. The linear concentration dependence plots of k_{obs} versus [Tu] for both first and second substitution steps for the Ru−Pt complexes are shown in Figure 2.

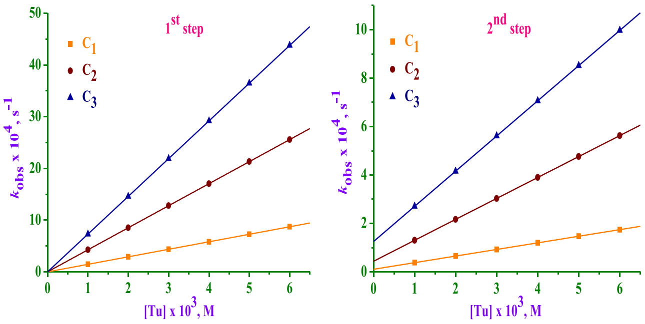

Figure 2. Straight line plots of k_{obs} versus [Tu] of all three Ru−Pt complexes. $[\mathbf{C_1}/\mathbf{C_2}/\mathbf{C_3}]$ = 50 μM, pH = 7.2 (5 mM Tris−HCl/50 mM NaCl) and *T* = 35 °C.

Table 1. Summary of the Rate Constants for Both First and Second Steps of the Reactions of the Ru−Pt Complexes with Nu at 35 °C[a]

		rate constants		
complex	Nu	$k_2{}^{1st} \times 10^1$, $M^{-1}\,s^{-1}$	$k_2{}^{2nd} \times 10^2$, $M^{-1}\,s^{-1}$	$k_{-1}{}^{2nd} \times 10^5$, s^{-1}
$\mathbf{C_1}$	Tu	1.45 ± 0.15	2.73 ± 0.10	1.04 ± 0.04
	L-Met	0.75 ± 0.11	0.37 ± 0.08[a]	
	5′-GMP	0.34 ± 0.09	0.75 ± 0.04	0.20 ± 0.02
$\mathbf{C_2}$	Tu	4.26 ± 0.21	8.65 ± 0.15	4.35 ± 0.09
	L-Met	1.75 ± 0.18	1.02 ± 0.15[a]	
	5′-GMP	0.96 ± 0.13	1.48 ± 0.08	0.84 ± 0.04
$\mathbf{C_3}$	Tu	7.57 ± 0.29	14.53 ± 0.22	10.99 ± 0.13
	L-Met	3.10 ± 0.26	2.08 ± 0.33[a]	
	5′-GMP	1.39 ± 0.15	2.20 ± 0.10	2.22 ± 0.04

[a] $k_1{}^{2nd} \times 10^4$, s^{-1}.

2.1.2. Reactions with L-Met. The biomolecule L-methionine (L-Met) is a thioether and an essential protein amino acid for humans, present in the blood which can react with the metal-based drugs. It forms Pt−S (thioether) drug reservoir intermediates that may be transformed into Pt−N7(GMP) of the DNA adduct.[24] L-Met substituted the chloride ligands of $\mathbf{C_1}/\mathbf{C_2}/\mathbf{C_3}$ in two successive substitution reactions because the kinetic traces gave excellent fits to a double-exponential function. The first step is very fast and shows a linear concentration dependence with zero intercepts on the *y*-axis. It is ascribed to the substitution of one chloride. The second step was found to be much slower, and the rate was found to be independent of the L-Met concentration. It is ascribed to a typical L-Met ring-closure reaction to form S, O-, or S, N−Pt chelates. Hence, the rate constant values for the first step

Scheme 3. Simplified Substitution Reaction Scheme for Ru−Pt Complexes with Different S-/N-Donor Nucleophiles, Nu = Tu, L-Met, and 5′-GMP

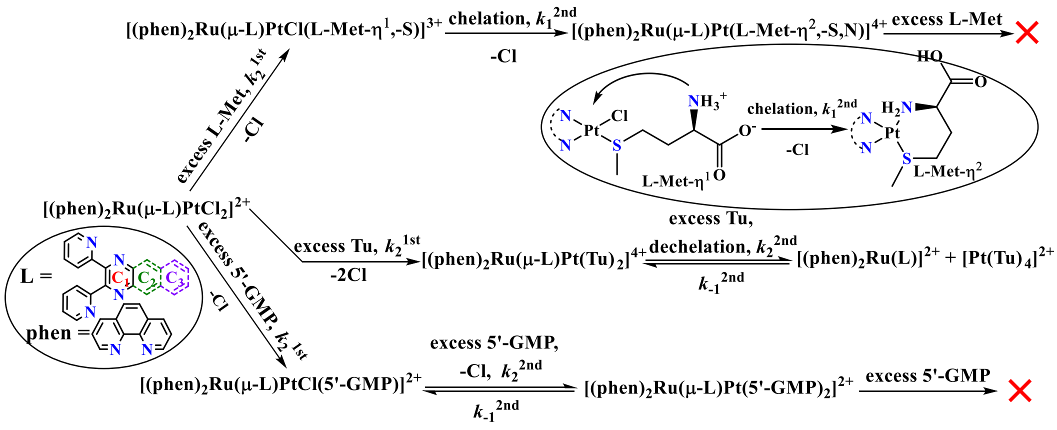

($k_2{}^{1st}$) are calculated according to the rate law $k_{obs}{}^{1st} = k_2{}^{1st}$ [Nu] (eq 1) from the slopes of linear dependence plots of $k_{obs}{}^{1st.}$ versus [L-Met], where $k_2{}^{1st}$ is the second-order rate constant, while the rate constant values for the second step ($k_1{}^{2nd}$) are found according to the rate law:

$$k_{obs}{}^{2nd} = k_1{}^{2nd} \tag{3}$$

where $k_1{}^{2nd}$ indicates the first-order rate constant. Linear concentration dependence plots of $k_{obs}{}^{1st.}$ versus L-Met concentration for the first step of the Ru−Pt complexes are shown in ESI Figure S2, and the rate data for both steps ($k_2{}^{1st}$ and $k_1{}^{2nd}$ values) at 35 °C are summarized in Table 1 while the other temperatures are given in ESI Tables S1 and S2. The ring closure of L-Met when substituting at the Pt(II) center and hence the observed independence of the rate on its concentration has been reported previously for similar reactions[25,26] (refer to Scheme 3 for the reaction pathway). At pH (= 7.2) of the reactions, L-Met ($pK_{-COOH} = 2.13$ and $pK_{NH_3} = 9.2$) occurs as a neutral species in its zwitterionic form and thus interacts with the complex via its S, N/O donor atoms.[27] The second step is less efficient than the amine (L-Met) due to the steric hindrance caused by the chelation of the first L-Met nucleophile.

2.1.3. Reactions with 5′-GMP. Biomolecule guanosine-5′-monophosphate (5′-GMP) consists of a 2′-ribose sugar and a phosphate moiety and is a component of the nucleobase guanine; it is a very good model ligand to assess for binding of metal ions to nucleobases of DNA via the N-donor atoms. It is well known that the metal ions can coordinate to 5′-GMP via both N1 and N7 atoms depending on the pH of the solution (see Scheme 2). Protonation of N1 reduces its availability in neutral and acidic solutions as its pKa (N1 free) value is 9.30 and this position is also sterically hindered by the amino group.[28]

The rate of substitution of chloride ligands of $\mathbf{C_1}/\mathbf{C_2}/\mathbf{C_3}$ by 5-GMP was studied at pH 7.2 (5 mM Tris−HCl/50 mM NaCl). The kinetics traces were good fits for the double-exponential functions, indicating the two-step substitution pathway. The first step shows a linear concentration dependence with zero intercepts on the y-axis. It can be ascribed to the formation of the $[(\text{phen})_2\text{Ru}(\mu\text{-L})\text{PtCl}(\text{N7})_{5'\text{-GMP}})]^{2+}$ intermediate complex. At pH 7.2, 5′-GMP remains as a non-protonated species and coordinates to the Pt(II) via its N7 donor (pKa (N7 free value is 2.48). Coordination via the N1 (pKa (N1 free) value is 9.30) is less likely due to the protonation.[29] This makes it less available in neutral and acidic solutions. Furthermore, the amino group sterically hinders this position. Hence, the rate is $k_{obs}{}^{1st} = k_2{}^{1st}$ [Nu], (eq 1). The substitution is slower compared to the reactions with Tu or L-Met due to the steric hindrance of 5′-GMP. The second step occurs at an even much slower rate and shows a small intercept on the y-axis. It involves the substitution of the second chloride by another incoming nucleophile, 5′-GMP according to the rate law $k_{obs}{}^{2nd} = k_2{}^{2nd}$ [Nu] + $k_{-1}{}^{2nd}$ (eq 2) as reported previously for similar complexes.[30,31] The observed intercepts can be attributed to the back reaction despite the excess chloride that was present in solution to prevent the spontaneous hydrolysis of the complex, where $k_2{}^{2nd}$ and $k_{-1}{}^{2nd}$ are the corresponding second- and first-order rate constants, respectively. This is probably owing to the increase in steric hindrance between the bulky intermediate, $[(\text{phen})_2\text{Ru}(\mu\text{-L})\text{PtCl}(5'\text{-GMP})]^{2+}$ and 5′-GMP. Furthermore, the space around the metal center is limited to replace the second chloride as it was already surrounded by a voluminous nucleophile, 5′-GMP. The substitution pathway is given in Scheme 3. Linear concentration dependence plots of k_{obs} versus [5′-GMP] for both first and second substitution steps of Ru−Pt complexes are given in ESI Figure S3. The rate data are summarized in Table 1 and ESI Tables S1 and S2.

The rate data (Table 1 and ESI Tables S1 and S2) show an increased reactivity of the Ru−Pt complexes successively from $\mathbf{C_1}$ to $\mathbf{C_3}$ as an increase in the π-conjugation on the spectator bridging ligand. This is the order of increase in the π-conjugation of the 2,3-bis(pyridyl)pyrazinyl bridges. As a result, the Pt(II) centers become more positive due to an increase in π-back bonding from the Pt 5d-orbitals into the extended π*-MOs of the chelate bridges. This leads to a smaller ΔE gap, which makes a metal-to-ligand charge transfer easier and then increases the reactivity from $\mathbf{C_1}$ to $\mathbf{C_3}$.[32] The π-back bonding further increases the electrophilicity of the Pt, leading to higher rates of substitution. The coordination of Ru at one end of each of the complexes enhances water solubility. Moreover, the charge addition of the two metal ions increases their reactivity toward substitution in addition to ensuring electrostatic interactions at target sites such as the DNA/BSA. Thus, increasing the reactivity order of the studied Ru−Pt complexes follows: $\mathbf{C_1} < \mathbf{C_2} < \mathbf{C_3}$.

The plots of k_{obs} versus [Nu] (Figure 3, ESI Figures S4 and S5) show a clear decreasing reactivity order of nucleophiles to replace the chloride of the complexes, which is Tu > L-Met >5′-GMP. Sulfur donor ligands are commonly coadministered with Pt(II) drugs to form Pt−S (thioether) intermediates that easily transform to Pt−N7 upon interaction with DNA.[33] Additionally, soft acidic metals like Pt(II)/Pd(II) exhibit a high affinity for soft bases such as S-donor nucleophiles, which leads to their faster reactivity.[34] Rate data presented in Table 1 and ESI Tables S1 and S2 support this argument well, as much higher rates for S-donor nucleophiles (Tu and L-Met) are observed in comparison to N-donor ligands (5′-GMP) for all three Ru−Pt complexes. Tu reacts faster than the other S-donor nucleophiles because it combines the ligand properties of thiolates (π-donors) and thioethers (σ-donors and π-acceptors).[35] Furthermore, the amine group enhances the nucleophilicity of S-atoms than the methyl group due to the positive inductive effect, which leads to faster reactivity of Tu with metal centers than the L-Met. It is also well known that the volume size of the nucleophile is inversely related to its reactivity; thus the bigger sized 5′-GMP reacts slower than the

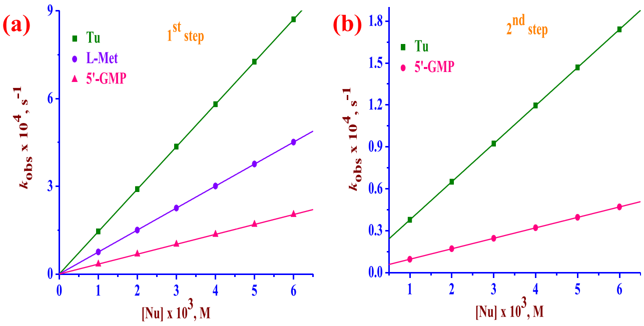

Figure 3. Linear plots of k_{obs} versus [Tu/L-Met/5′-GMP] for both the first (a) and second steps (b) of the complex $\mathbf{C_1}$. [$\mathbf{C_1}$] = 50 μM, pH = 7.2 (5 mM Tris−HCl/50 mM NaCl), and T = 35 °C.

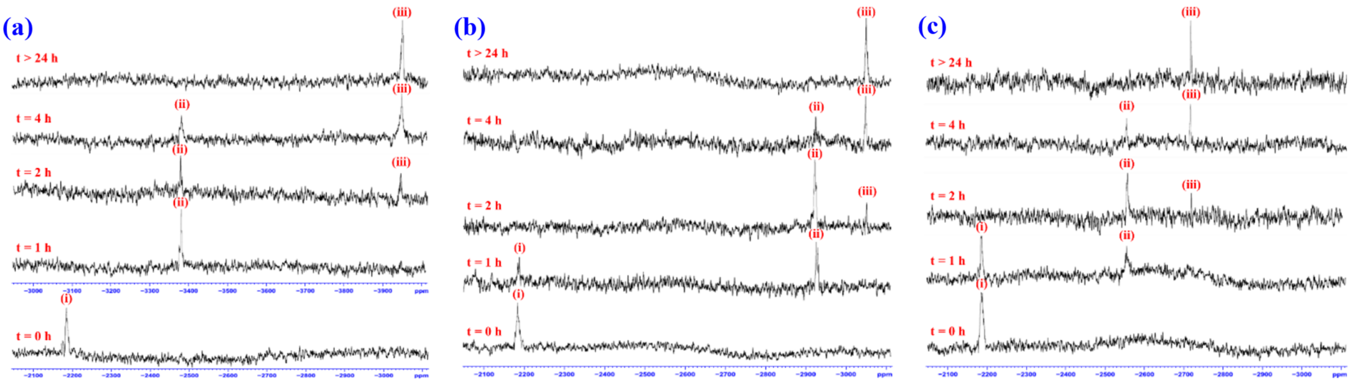

Figure 4. Time-dependent ^{195}Pt NMR chemical shifts of **C1** with six times equivalents of Tu (a), L-Met (b), and 5′-GMP (c) in 50% DMF-d^7.

other studied nucleophiles. On the other hand, Tu is the least sterically demanding molecule and hence substitutes with the higher rates. Thus, the reactivity trend (Tu > L-Met >5′-GMP) of these nucleophiles with the studied Ru−Pt complexes is well consistent with previous studies.[36,37]

2.2. Temperature Effect and *Iso*-Kinetic Relationship. The Eyring equation was used to compute activation parameters ($\Delta H^{\#}$, $\Delta S^{\#}$, and $\Delta G^{\#}$) for all the reactions and values presented in ESI Table S3, and the plots are given in ESI Figures S6 and S7. From the data, it is found that both the first and second steps are proposed to follow an associative mechanism which is established by the relatively large negative entropy of activation ($\Delta S^{\#}$) and low positive enthalpy of activation ($\Delta H^{\#}$) values. These values signify that the transition states are energetically favorable to forming more ordered transition states with incoming nucleophiles than the reactants.[38] Thus, $\Delta H^{\#}$ and $\Delta S^{\#}$ values support an associatively activated substitution mechanism at the square-planar Pt(II) centers of the complexes. However, the magnitudes of Gibbs free energy ($\Delta G^{\#}_{35\ °C}$) values for the reactions of the three different Ru−Pt complexes with three different nucleophiles are comparable for the first step of substitution, signifying that these reactions essentially follow the same associative mechanism. Furthermore, a linear free energy relationship (LFER) was tested by plotting $\Delta H^{\#}$ versus $\Delta S^{\#}$ (refer to ESI Table S3 for data). ESI Figure S8 depicts a linear isokinetic plot with a positive slope and intercept. The slope and intercept of the plot give the *iso*-kinetic temperature (446 K) and Gibbs free energy (103 kJ mol^{-1}), respectively. The observed LFER/isokinetic plot further signifies the similarity in mechanism for the first chloride substitution of all the reactions associated.

2.3. Product Characterization by ^{195}Pt Nuclear Magnetic Resonance (NMR) Spectroscopy. The kinetic reaction pathways of $\mathbf{C_1}$ with each nucleophile Nu were studied by ^{195}Pt NMR spectroscopy as a model reaction for the other Ru−Pt complexes. Because the resonance frequency (chemical shifts) of the ^{195}Pt nuclide for square-planar complexes depends on the coordinated donor atoms on the Pt, ^{195}Pt can be used to probe the coordination details of square-planar Pt complexes. The chemical shift for the ^{195}Pt metal center depends on the σ-donor/π-acceptor nature and the increasing order follows among coordinating atoms in the complex and nucleophiles is Cl < N < S.[39−41] Each nucleophile (about 6 times equivalent to that of $\mathbf{C_1}$) was dissolved in D_2O while the complex, $\mathbf{C_1}$ (10 mg), was dissolved in 500 μL DMF-d^7 due to its lower solubility in D_2O. The observed ^{195}Pt NMR spectrum of $\mathbf{C_1}$ before the addition of Nu showed that the Pt chemical shift at $\delta = -2186$ ppm (Figure 4) agrees with data for Pt(II) ions coordinated by two chelated nitrogen atoms and two chloride atoms in a square-planar manner, viz. Pt(N^N)Cl_2 species.[23] The Pt(II) chemical shifts were monitored over the period of 72 h after mixing $\mathbf{C_1}$ with more than 6 times equivalents of each Nu (4.5, 8.7, and 23.7 mg of Tu, L-Met, and 5′-GMP, respectively, in 500 μL D_2O).

2.3.1. Reaction Products with Tu. Figure 4a shows the spectral changes after the addition of six times equivalents of Tu to $\mathbf{C_1}$; it can be seen that the reactant peak 4a(i) disappeared and appeared as a new peak 4a(ii) at −3381 ppm. This peak appeared in the range from $\delta = -3150$ to -3550 ppm,[41,42] more precisely at $\delta = -3400$ ppm[43] indicating the formation of species like Pt(N^N)S_2. The formation of this species is most likely due to the simultaneous substitution of two chlorides by S-donor Tu nucleophiles. Notably, no peaks were obtained which corresponded to Pt coordinated with two nitrogen atoms, one S-donor molecule and one chloride atom viz., Pt(N^N)SCl which normally appear in the range between $\delta = -2891$ and -3159 ppm[44] (contrast to the peak 5b, ^{195}Pt $\delta = -2924$ ppm for the same species vide infra when $\mathbf{C_1}$ reacts with L-Met). Moreover, the present peak 4a(ii) appeared at up field (^{195}Pt $\delta = -3381$) owing to coordinating the more σ-donor/π-acceptor atom to the Pt metal as stated vide infra (S is a strong σ-donor/π-acceptor than Cl) supporting the formation of Pt(N^N)S_2 species rather than Pt(N^N)SCl. The absence of a peak corresponding to Pt(N^N)SCl may also be due to the absence of stepwise substitution of two chlorides by incoming Tu, or the formed intermediate is quite unstable to monitor due to the lower signal-to-noise ratio. This prevents the direct observation of the formation of some intermediate species; we can only assume a relatively stable intermediate species. With time, peak 4a(ii) intensity decreases and disappears completely, while a new peak 4a(iii) shows at up field $\delta = -3947$ ppm. This signal typically falls in the range (−3800 to −4150 ppm[45,46]) for the species like PtN_4. Thus, this indicates that the strong nucleophilicity of Tu forced the decoordination of the spectator ligand moiety from the Pt(II) to give a $Pt(Tu)_4^{2+}$ and a free 2,3-di(2-pyridyl)quinoxaline ligand (bpq) as final products; similar results were reported for similar Pt(II) complexes earlier.[23] Furthermore, the peak 4a(iii) is unaffected even when the reaction is allowed for more than 2 days endorses the formation of $Pt(Tu)_4^{2+}$ as an ultimate final product of the reaction of $\mathbf{C_1}$ with Tu. This was further supported by X-ray diffraction (XRD) analyses of the crystal obtained from the same sample after 7 days; details are given vide infra.

2.3.2. Crystal Structure of Pt(Tu)$_4$. After the product analysis of the reaction between $\mathbf{C_1}$ and Tu in 50% DMF by ^{195}Pt NMR in the NMR tube was left for several days at room temperature, orange red crystal blocks grew onto the walls of the tube. XRD analysis confirmed the crystal product as a salt of the $[Pt(Tu)_4]^{2+}$, for the crystal structure see Figure 5. This was not surprising given the strong substitution nucleophilicity of Tu and hence its potential to decoordinate ligand off the Pt(II) square plane of the Ru−Pt complexes. This has already been explained vide supra in the discussion of the ^{195}Pt NMR spectral changes recorded during the progression of one of the reactions. The product of the reaction crystallized as a mixed chloride/perchlorate salt, $[Pt(Tu)_4]Cl{\cdot}ClO_4{\cdot}2NH_2(CH_3)_2$ molecule. Figure 5 depicts an ORTEP view (50% probability) of the crystal structure (also refer to ESI Figure S9 for a full crystal structure with solvent molecules). The DMF was likely reduced by the chloride ions to dimethyl amine and carbon monoxide. Subsequently, the former molecule rearranged to form unusual $NH_2(CH_3)_2$ species while the latter compound further reacted with chloride ions to form the perchlorate ions; similar results have been reported in the literature.[47,48] Eventually, they cocrystallized with the $[Pt(Tu)_4]^{2+}$ ions as confirmed in the solid-state X-ray structure of the ultimate salt product from the reaction between $\mathbf{C_1}$ and Tu. The counter ions (one ClO_4^- and one Cl^- ions) remind the charge of the product is +2 which confirms the typical square-planar geometry of the P(II) compounds. Details of data collection and refinement are provided in ESI Table S4, whereas the selected bond lengths, bond angles, and torsional angles are shown in Table 2.

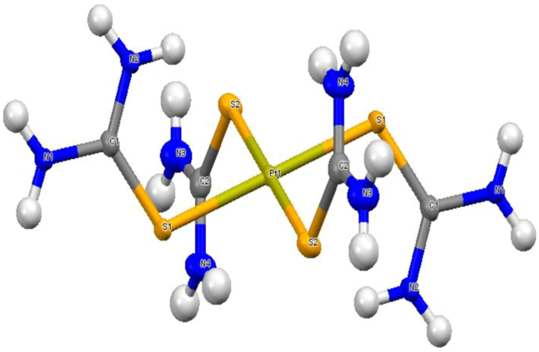

Figure 5. Molecular structure (thermal ellipsoids at 50%) of the $[Pt(Tu)_4]^{2+}$; counter ions were omitted for clarity.

2.3.3. Reaction Products with L-Met. Figure 4b shows the spectra that were recorded before and after $\mathbf{C_1}$ was mixed with L-Met (6 times equivalents). Before mixing, $\mathbf{C_1}$ resonated at $\delta = -2186$ ppm, within 1 h after the reaction, the intensity of peak 4b(i) decreases while a new peak 4b(ii) appears at $\delta = -2924$ ppm, indicating the formation of new species, [(phen)$_2$Ru(μ-L)PtCl(L-Met-η1, -S)], through the substitution of chloride by incoming S-donor Nu, L-Met as depicted in Scheme 3 (*vide supra*). This intermediate further reacts slowly (>24 h) to form a new product that features a peak of 4b(iii) at $\delta = -3051$ ppm. However, the chemical shift of the second product falls upfield to the range ($\delta = -3200$ to 3500 ppm[43,44] for Pt(N^N)S$_2$. This is an indication the second chloride is substituted by the N atom of coordinated L-Met via ring closure, rather than by an S-atom from another L-Met molecule. The chemical shift ($\delta = -3051$ ppm) of this Pt(N^N)(S^N) species is within the range ($\delta = -2798$ to -3213 ppm)[44,49,50] reported for other PtN$_3$S species. The intensity of its chemical shift (4b(iii)) did not change even after leaving the reaction for more than 24 h, making it the ultimate product of the reaction which is [(phen)$_2$Ru(μ-L)Pt(L-Met-η2, -S,-N)] species.

2.3.4. Reaction Products with 5′-GMP. Figure 4c depicts the spectra that were recorded before and after the reaction between $\mathbf{C_1}$ and 5′-GMP (six times equivalents). The reactant peak 4c(i) intensity starts to decrease with time while a new peak 4c(ii) appears at $\delta = -2555$ ppm, which fall within the range $\delta = -2215$ to -2579 ppm signifying that the Pt coordinated with three N-atoms and one Cl atom, viz., PtN$_3$Cl.[41,44] This indicates the formation of new species, Pt(N^N)NCl as a result of the substitution of one chlorine atom by 5′-GMP. With time, peak 4c(ii) vanished completely and appeared as a new peak 4c(iii) at $\delta = -2718$ ppm, and it remains unchanged even after 48 h, ratifying the absence of further reaction. Moreover. the peak 4c(iii) is in the range between $\delta = -2145$ and -2795 ppm, indicating that Pt is coordinated with four N-atoms.[44,50,51] Thus, it is clear that peak 4c(iii) is due to the replacement of the second chloride by another incoming 5′-GMP molecule to form Pt(N^N)N$_2$ species as the sole final product of the reaction of $\mathbf{C_1}$ with 5′-GMP also corroborates with the UV−visible absorption kinetic results.

2.4. Binding Activities. *2.4.1. CT-DNA Interactions.* Vital information about the DNA such as mutation, transportation, and replication helps to understand its role in cellular functions notably for cancer by considering DNA−drug interactions. These interactions are attained through the noncovalent and covalent interactions by forming DNA−drug adducts. However, in most cases the metal complex−DNA adduct interactions are likely to be a noncovalent type such as intercalation, major/minor groove, and external electrostatic binding modes.[52] In a groove-bound mode, DNA binds to the metal complex to form intrastrand and interstand cross-links such as electrostatic, hydrogen bonding, and hydrophobic $\pi-\pi$ stacking interactions[53,54] Bindings into the groove have significantly higher DNA sequence efficiency and selectivity,

Table 2. Selected Experimental (XRD) Geometrical Parameters for the $[Pt(Tu)_4]^{2+}$

bond lengths (Å)		bond angles (°)		torsion angles (°)	
Pt−S1	2.3224(9)	S1−Pt−S1^{1}	180.0	Pt−S1−C1-N1	−176.0(3)
Pt−S1^{1}	2.3224(9)	S2−Pt−S2^{1}	180.0	Pt−S1−C1-N2	4.6(4)
Pt−S2	2.3330(10)	S1−Pt−S2	92.94(3)	Pt−S2−C2-N4	−0.4(4)
Pt−S2^{2}	2.3330(10)	S2−Pt−S1^{1}	87.06(3)	Pt−S2−C2-N3	179.8(3)
		S1^{1}−Pt−S2^{1}	92.94 (3)		
		S2^{1}−Pt−S1	87.06(3)		

whereas DNA conformational changes create a binding cavity, which leads to intercalation. The majority of drugs bound into groove and intercalating have a preference for binding to AT (adenine/thymine)-rich and GC (guanine/cytosine)-rich regions, respectively. The interactions could be assigned experimentally using absorption spectral titration.

2.4.1.1. UV–Visible Absorption Studies. The interactions between Ru–Pt heterometal complexes and duplex CT-DNA were studied by measuring the changes in absorbance when CT-DNA was added to a fixed concentration of each Ru–Pt complex, and the results are shown in ESI Table S5. Figure 6 depicts a typical graph of the spectral changes caused by $\mathbf{C_1}$–CT-DNA interactions. For similar spectral changes of $\mathbf{C_2}$ and $\mathbf{C_3}$ complexes along with the inset of Wolfe–Shimmer plots, see ESI Figures S10a and S10b, respectively. The spectra of three Ru–Pt complexes revealed a common hypochromic shift of λ_{max} with each addition of CT-DNA, owing to π–π stacking interactions between each Ru–Pt complex's aromatic chromophores and CT-DNA base pairs which are reliable to the intercalative binding mode of interactions.[55] However, the strength of interactions can be examined by computing intrinsic binding constant, K_b values[56] from the ratio of the slopes to intercepts of the Wolfe–Shimmer plot, values of which are presented in Table 3. It is found that the magnitudes of binding constants are in the order of 10^5 M, indicating that the Ru–Pt complexes prefer to intercalate noncovalently between the base pairs of CT-DNA. The complex $\mathbf{C_3}$ has shown the highest binding affinity toward CT-DNA followed by $\mathbf{C_2}$ and $\mathbf{C_1}$ indicating that the binding ability increases with increasing π-surface on the bridging ligand which facilitates stronger noncovalent π–π stacking interactions with CT-DNA as a result of stronger intercalation mode of binding interaction for $\mathbf{C_3}$ than the other two Ru–Pt complexes. Furthermore, ΔG values for the reaction between each complex and CT-DNA were computed using the Van't Hoff equation ($\Delta G = -RT \ln K_b$). Values were found to be −30 ± 3, −35 ± 2, and −36 ± 3 kJ mol^{-1} for $\mathbf{C_1}$, $\mathbf{C_2}$, and $\mathbf{C_3}$, respectively. Negative ΔG values indicate the spontaneity of binding of complexes with DNA, as well, as the order of magnitude increases with the respective structure of the Ru–Pt complex. This signifies that the complex $\mathbf{C_3}$ has shown stronger binding in comparison to $\mathbf{C_2}$ and $\mathbf{C_1}$, and the decreasing order follows $\mathbf{C_1} < \mathbf{C_2} < \mathbf{C_3}$.

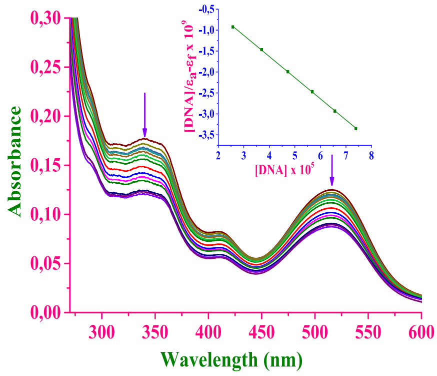

Figure 6. UV–vis spectral changes of $\mathbf{C_1}$ (14 μM) in 5 mM Tris–HCl/50 mM buffer at pH 7.2 with CT-DNA (0–90 μM). The arrow shows how absorbance decreases as CT-DNA concentration increases. Inset: Wolfe–Shimmer plot of [CT-DNA] versus [DNA]/($\varepsilon_a - \varepsilon_f$).

2.4.1.2. Fluorescence Quenching Studies. It is well known that EtBr is an intercalator, intercalating with CT-DNA through its planar phenanthroline ring to form an EtBr+CT-DNA adduct which is easily detected by fluorescence spectroscopy in the emission spectrum of EtBr upon addition of CT-DNA, and the data are shown in ESI Table S6. In the absence and presence of increasing amounts of each Ru–Pt complex ($\mathbf{C_1}$/$\mathbf{C_2}$/$\mathbf{C_3}$), the fluorescence emission spectra of the EtBr + CT-DNA adduct were monitored at 596 nm after excitation at 510 nm. It is noted that the studied Ru–Pt complexes do not fluoresce in the monitored range either in the absence or presence of CT-DNA when excited at 510 nm. Furthermore, no new peaks were observed after the addition of each Ru–Pt complex to the EtBr indicating that EtBr did not provoke quenching of its free fluorescence emission, signifying that the complexes did not bind to EtBr. The addition of increasing amounts of each Ru–Pt complex to the fixed concentration of EtBr + CT-DNA adduct resulted in a significant decrease in the intensity of the 596 nm band, which indicated that the studied Ru–Pt complexes were able to displace bound EtBr from CT-DNA.

Representative spectra of quenched emission intensities with a notable bathochromic (red) shift by the addition of a complex $\mathbf{C_1}$ to the 20.0 μM of a fixed concentration of EtBr bound to CT-DNA are given in Figure 7a and also see ESI

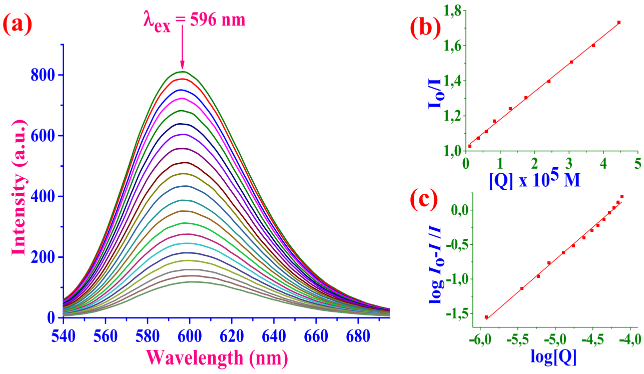

Figure 7. (a) Fluorescence emission spectra of EtBr bounded to CT-DNA in the presence of $\mathbf{C_1}$: [EtBr] = 20.0 μM, [CT-DNA] = 20.0 μM, and [$\mathbf{C_1}$] = 0–150 μM. The arrow shows the decrease in intensity with increasing the $\mathbf{C_1}$ concentration. (b) Stern–Volmer plot of I_o/I versus [Q] and (c) Scatchard plot of log[(I_o − I)/I] versus log[Q].

Table 3. Binding Constants and Quenching Constants for Ru–Pt Complexes ($\mathbf{C_1}$, $\mathbf{C_2}$, and $\mathbf{C_3}$) with CT-DNA

	UV titration	fluorescence EtBr exchange titration				
complex	$K_b \times 10^{-5}$, M^{-1}	$K_{sv} \times 10^{-4}$, M^{-1}	$K_{app} \times 10^{-6}$, M^{-1}	$k_q \times 10^{-12}$, M^{-1} s^{-1}	$K_F \times 10^{-4}$, M^{-1}	n
$\mathbf{C_1}$	1.30 ± 0.11	1.59 ± 0.07	3.33 ± 0.11	0.69 ± 0.19	1.00 ± 0.05	0.99 ± 0.04
$\mathbf{C_2}$	7.68 ± 0.16	2.83 ± 0.13	6.25 ± 0.17	1.23 ± 0.24	1.98 ± 0.11	0.99 ± 0.05
$\mathbf{C_3}$	14.0 ± 0.23	3.92 ± 0.19	8.00 ± 0.23	1.70 ± 0.31	3.96 ± 0.17	1.00 ± 0.07

Figures S11a and S12a for changes that occur on the displacement of EtBr from the base pair of CT-DNA by the other two complexes, $\mathbf{C_2}$ and $\mathbf{C_3}$, respectively. The quenching data were fitted to the Stern−Volmer equation ($I_o/I = 1 + K_{SV}[Q]$, representative straight line plot for $\mathbf{C_1}$ is given in Figure 7b and the plots for $\mathbf{C_2}$ and $\mathbf{C_3}$ are given in ESI Figures S11b and S12b, respectively) which gave Stern−Volmer quenching constant, K_{sv} (values are given in Table 3). The magnitude of K_{sv} (10^4 M^{-1}) suggests that the Ru−Pt complexes can competitively exchange EtBr off the DNA medium, most likely via an intercalative mode of binding. The apparent binding constant, K_{app}, was computed using the equation: $K_{EtBr}[EtBr] = K_{app}[Q]$ with values ranging from 3.3 to 8.0 × 10^6 M^{-1} (see Table 3). It was noticed that the computed K_{app} values are less than the classical intercalators' and metallointercalators' binding constant (10^7 M^{-1}).[57] This signifies that the observed quenching of CT-DNA-EtBr by the studied Ru−Pt complexes is likely to be due to the intercalative mode of interaction. The bimolecular quenching rate constant, k_q values were also computed using the Stern−Volmer equation ($K_{SV} = k_q\tau_0$), ranging from 0.7 to 1.7 × 10^{12} M^{-1} s^{-1} (refer to Table 2), which are higher than those of the dynamic (biopolymeric) quenchers (∼10^{10} M^{-1} s^{-1}), implying that EtBr was displaced from the CT-DNA statically rather than dynamically.[55] Scatchard plots also gave the binding constant K_F, and the number of binding sites '*n*' values were determined from the Scatchard equation $\log(I_o - I)/I = \log K_F + n \log[Q]$, a typical linear plot for complex $\mathbf{C_1}$ is given in Figure 7c, and the plots for $\mathbf{C_2}$ and $\mathbf{C_3}$ are given in ESI Figures S11c and S12c, respectively. From the data presented in Table 3, it is clear that the complex $\mathbf{C_3}$ had the highest affinities for CT-DNA. Furthermore, the decrease in the relative fluorescence emission intensity of EtBr + CT-DNA by the addition of each Ru−Pt complex realizes that $\mathbf{C_3}$ has shown the highest efficiency (see Figure 8), which is in line with their binding abilities. The ability of complexes to compete with EB and bind with CT-DNA via intercalation was demonstrated by a reasonable quenching in fluorescence intensity (up to 80% of the initial EB−DNA fluorescence).[58] Also, the results are in excellent agreement with data obtained from the UV−vis spectral studies, signifying that the Ru−Pt complexes significantly interact with DNA intercalatively, and the ascending order of their binding ability follows: $\mathbf{C_1} < \mathbf{C_2} < \mathbf{C_3}$.

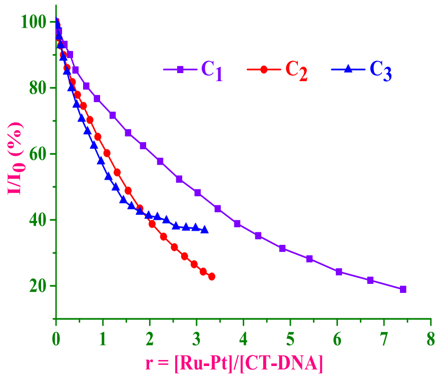

Figure 8. Relative intensity of the fluorescence emission of EtBr + CT-DNA at λ_{em} = 596 nm (λ_{ex} = 510 nm) versus [Ru−Pt]/[CT-DNA] for each Ru−Pt complex ($\mathbf{C_1}$, $\mathbf{C_2}$, and $\mathbf{C_3}$) in 5 mM Tris/50 mM NaCl, pH = 7.2. (Decrease in initial EtBr+CT-DNA fluorescence up to 19% for $\mathbf{C_1}$, 23% for $\mathbf{C_2}$, and 37% for $\mathbf{C_3}$.)

2.4.2. Viscometric Studies.

Viscosity measurements of CT-DNA and variable amounts of the Ru−Pt metal complexes and EtBr were recorded to inspect the changes in the CT-DNA helical structure. Intercalative associations lengthen/separate the DNA helix to accommodate the intercalating molecule, resulting in increased CT-DNA viscosity. Nonclassical intercalators cause a bend or kink in the CT-DNA helix, reducing its length and thus maintaining its viscosity.[59] The measured viscosities have remained almost constant. The relative specific viscosity (η/η_0), where η and η_0 are the specific viscosities of CT-DNA in the presence or absence of the test complexes, was computed for the solutions containing an increasing concentration of each Ru−Pt complex ($\mathbf{C_1}$, $\mathbf{C_2}$, and $\mathbf{C_3}$) in CT-DNA in 5 mM Tris−HCl/50 mM NaCl, pH 7.2 ranging from 1.0 to 7.0 mM and plotted against [Ru−Pt]/[DNA] (ESI Figure 13). The relative specific viscosity of CT-DNA increased on the incremental addition of each Ru−Pt complex and was even higher than that for the classical intercalator EtBr, which showed the strong intercalative mode of binding which is consistent with our foregoing postulation. The complex $\mathbf{C_3}$ had the strongest interactions with CT-DNA and the decreasing order followed $\mathbf{C_3} > \mathbf{C_2} > \mathbf{C_1}$. This is well corroborated with the experimental results obtained from the spectroscopic studies.

2.4.3. BSA Interactions.

BSA is structural homology to human serum albumin which is the most abundant protein in the blood plasma that transports ions/proteins to the cells and tissues.[60,61] BSA has two high fluorescence tryptophan residues, namely, Trp-134 embedded in the IB subdomain, exposed to a hydrophilic environment and Trp-214 is in the IIA subdomain, deeply buried in the hydrophobic loop of the protein; moreover, the quenching effects of these two residues are minimum.[62] The fluorescence of tryptophan in BSA is mainly owing to the residue located in a hydrophobic cavity. Thus, it is very important to simulate possible binding interactions with studied Ru−Pt complexes.

2.4.3.1. UV−Visible Absorption Studies.

The fluorescence quenching mechanisms are typically classified as either static or dynamic. The type of quenching can be revealed from UV−vis absorption spectral studies. The UV−vis spectra of BSA in the absence and presence of each Ru−Pt complex are shown in ESI Figure S14. The BSA absorption intensity is enhanced with a prominent blue shift by the addition of each Ru−Pt complex ($\mathbf{C_1}/\mathbf{C_2}/\mathbf{C_3}$) which indicates that the interactions between BSA and studied Ru−Pt complexes are static rather than dynamic.[43]

2.4.3.2. Fluorescence Quenching Studies.

Fluorescence spectroscopic titration is another effective procedure for determining the mode of interactions and binding affinities of Ru−Pt metal complexes with BSA. The emission profile by the addition of aliquots of different concentrations of complexes $\mathbf{C_1}$−$\mathbf{C_3}$ into a BSA solution (1.08 μM) quenches its fluorescence emission band at λ_{em} = 348 nm. Noticeable BSA quenching by the addition of each Ru−Pt complex may be ascribed to changes in the tryptophan environment of BSA as a result of the binding of the complex to the BSA.[63]

A decrease in emission intensity with a little blue shift at λ_{em} (348 nm) of BSA indicates the associative interaction between the BSA and quenchers, Ru−Pt complexes (see Figure 9a for $\mathbf{C_1}$ for representative and ESI Figures S15a and S16a for other Ru−Pt complexes for spectral over quencher). The change in intensity data with the sequential addition of each complex fitted well into the Stern−Volmer equation. The Stern−Volmer quenching constant, K_{sv}, was calculated from the

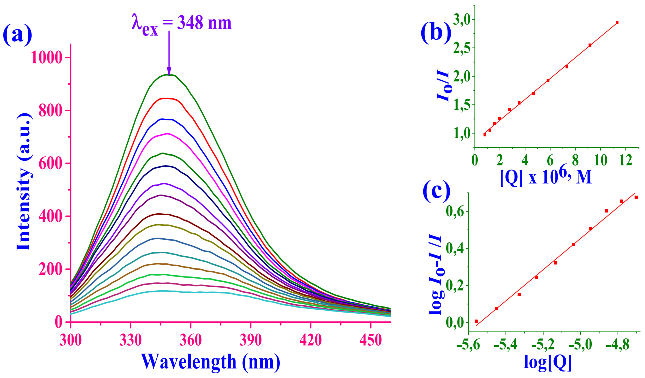

Figure 9. (a) Fluorescence emission spectra of BSA in the absence and presence of $\mathbf{C_1}$: [BSA] = 1.08 μM and [$\mathbf{C_1}$] = 0–20 μM. The arrow shows the decrease in intensity with increasing the $\mathbf{C_1}$ concentration. (b) Stern–Volmer plot of I_o/I versus [Q] and (c) Scatchard plot of log[$(I_o - I)/I$] versus log[Q].

slopes of linear plots of I_o/I versus [Q] (refer to Figure 9b for the linear Stern–Volmer plot for $\mathbf{C_1}$ also ESI Figures S15b and S16b for other two complexes). The bimolecular quenching constants, k_q value were also computed using the equation $K_{SV} = k_q\tau_0$, and the values of k_q and K_{sv} are shown in Table 4. The Scatchard equation was used to compute the binding constant, K_F and number of binding sites, *n*, and the results are summarized in Table 4. Typical Scatchard plots of log$(I_o - I)/I$ versus [Q] for $\mathbf{C_1}$ are shown in Figure 9c; for $\mathbf{C_2}$ and $\mathbf{C_3}$ complexes, refer to ESI Figures S15c and S16c, respectively. The magnitudes of K_F values (10^5 M^{-1}) are high, signifying that the binding abilities of complexes with BSA are most likely owing to hydrophobic interactions and the sites are located in subdomain IIA of BSA.[64] The analyzed *n* values for all three Ru–Pt complexes are close to 1 (see Table 4), suggesting that the complexes are bound to BSA via a single binding site. Furthermore, the slopes of Figure 10 and the obtained K_F values indicated that complex $\mathbf{C_3}$ is the strongest BSA binder than the other two complexes and their binding affinities decrease in the order: $\mathbf{C_3} > \mathbf{C_2} > \mathbf{C_1}$.

Table 4. Binding Constant, Quenching Constants, and Number of Binding Sites for the Ru–Pt with BSA

complex	$K_{sv} \times 10^{-5}$, M^{-1}	$k_q \times 10^{-13}$, M^{-1} s^{-1}	$K_F \times 10^{-5}$, M^{-1}	*n*
$\mathbf{C_1}$	1.84 ± 0.08	1.84 ± 0.16	0.47 ± 0.06	0.84 ± 0.03
$\mathbf{C_2}$	2.26 ± 0.15	2.26 ± 0.24	1.16 ± 0.10	1.00 ± 0.05
$\mathbf{C_3}$	2.65 ± 0.22	2.65 ± 0.33	6.64 ± 0.17	1.01 ± 0.07

From results from Tables 3 and 4, it is clear that these Ru–Pt complexes have considerable binding affinities to both CT-DNA and BSA. Thus, these Ru–Pt complexes bind to CT-DNA in intercalative binding mode (supported by both UV–vis and fluorescence real time data), whereas the hydrophobic interactions are accountable for the BSA. However, the $\mathbf{C_3}$ complex shows the greatest DNA and BSA binding affinity owing to the extended π-surface on its bridged ligand. The π-surface of the ligand increases as the order of the binding abilities of the complexes and the decreasing binding order is $\mathbf{C_3} > \mathbf{C_2} > \mathbf{C_1}$. The rate of aqua substitution with S/N-donor nucleophiles (Tu, L-Met, and 5-GMP) follows the same order of reactivity; thus, the binding affinities are in line with the kinetic results.

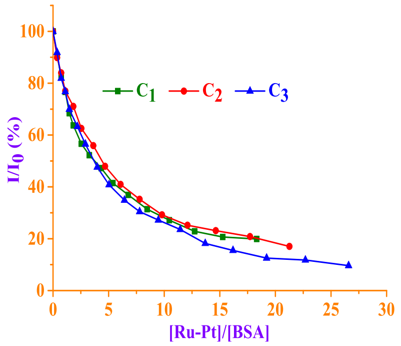

Figure 10. Relative intensity of the fluorescence emission of BSA at λ_{em} = 348 nm versus [Ru–Pt]/[BSA] for each Ru–Pt complex ($\mathbf{C_1}$, $\mathbf{C_2}$, and $\mathbf{C_3}$) in 5 mM Tris/50 mM NaCl, pH = 7.2. (Decrease in initial BSA fluorescence up to 20% for $\mathbf{C_1}$, 17% for $\mathbf{C_2}$, and 10% for $\mathbf{C_3}$.)

2.5. Concentration-Dependent Photoinduced Cleavage Activities.

2.5.1. pcDNA Cleavage Studies. The majority of anticancer metallodrugs that interact with DNA are known to cause DNA strand scission. Thus, we investigated the ability of the Ru–Pt complexes to cleave DNA using supercoiled, SC pcDNA followed by gel electrophoresis of the nicked circular, NC and relaxed linear, LC DNA forms. The substrate was incubated with complexes in a medium of 1.0 × TAE buffer (40 mM Tris acetate/1 mM EDTA, pH = 8.3) under physiological conditions. In general, when pcDNA interacts with metal complexes it can be converted from supercoiled, SC form (form I) to a relaxed nicked circular, NC form (form II) implicating single-strand DNA scission. Agarose gel electrophoresis can separate these forms because the latter migrates much faster; however, the appearance of the linearized, LC form (form III) of DNA between form I and form II suggests that both the strands of DNA are cleaved which suggests the lethal double-strand scission.[65] Concentration- and time-dependent cleavage experiments of Ru–Pt complexes pcDNA were carried out, and forms were separated by the gel electrophoresis method. The amounts of the supercoiled (SC) and nicked circular (NC) forms on the addition of each of these complexes to pcDNA were quantified by densitometry. Data are listed in ESI Table S7, and the cleavage bands of pcDNA at different concentrations of the complexes are given in Figure 11. Lane 0 is for the control and lanes 1–6 are for the concentration gradient ranging from 10 to 250 μM. The results demonstrate that all of the three Ru–Pt complexes can cleave pcDNA in a concentration-dependent manner.

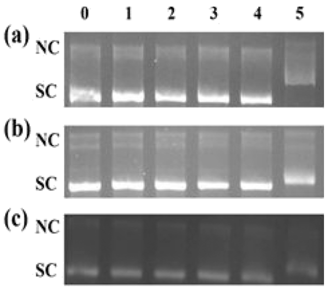

Figure 11. 37 °C Agarose gel electrophoresis of pcDNA (supercoiled) cleavage by Ru–Pt complexes. Lane 0, 0.1 μM DNA control; lanes 1–5, respective complex (10, 25, 50, 100, and 250 μM) + 0.1 μM DNA. (a) $\mathbf{C_1}$; (b) $\mathbf{C_2}$; and (c) $\mathbf{C_3}$.

Complex C_1 (~24%) has shown relatively higher activity than the complex C_2 (~18%) and C_3 (~17%) at 250 μM (refer to Figure 12 and ESI Table S7). This fact can be attributed to the high rate of nucleophilic substitution due to the extended π-surface on the core ligand of the complex. Thus, the order of relaxing pcDNA could be concluded as $C_1 < C_2 \sim C_3$. Because the DNA cleavage abilities of the Ru−Pt complexes are related to their DNA binding abilities, it may be that the complexes induce DNA cleavage by loosening the SC form. This trend inversely collaborated with their binding abilities, which supports their order of interactions with DNA.

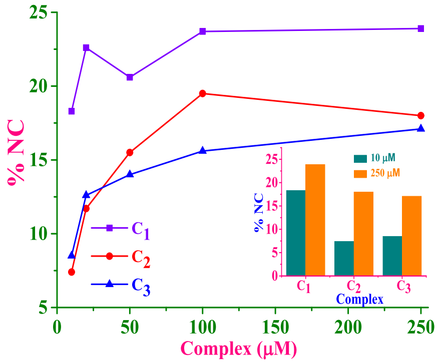

Figure 12. Cleavage of pcDNA at different concentrations of Ru−Pt complexes [10−250 M in 40 mM Tris acetate/1 mM EDTA, pH = 8.3 containing 1% DMF] was exposed for 30 min to UV light at 350 nm (84 W). The inset shows a bar diagram representation of the percent NC of various complexes at 10 and 250 M.

2.5.2. BSA Cleavage Studies. As the Ru−Pt complexes (C_1, C_2, and C_3) exhibited good binding affinity toward BSA, we studied dose-dependent photoinduced cleavage of BSA (4 μM) by the complexes in 50 mM Tris−HCl buffer. The cleaved fragments were separated by SDS-PAGE gel electrophoresis and stained by the Coomassie blue protocol at 27 °C temperature on photoexposure to UV-A light (6 W) at 365 nm. The gel profile for the cleavage product of the complex C_1 is given in Figure 13 as a representative image, and see ESI Figures S16a and S16b for C_2 and C_3, respectively. Figure 14 shows concentration-dependent photoinduced cleavage of BSA (4 μM) at different concentrations of the complexes. The BSA control is in lane 10 in Figure 13, ESI Figures S17a and S17b for C_1, C_2, and C_3, respectively indicating no apparent cleavage for BSA under the same conditions. No fading or smearing of the BSA band for complexes C_1−C_3 was noticed, indicating that no cleavage for BSA occurred similar to that reported for Cu(II) complexes.[66] Moreover, the densitometry analysis of photoinduced BSA revealed that lower concentrations of complexes show very less cleavage (less than ~20%) which is almost similar to the cleavage that occurred even at higher concentrations of 500 μM for all three complexes (Figure 14). This suggests that all three complexes have similar photoinduced BSA cleavage activity.

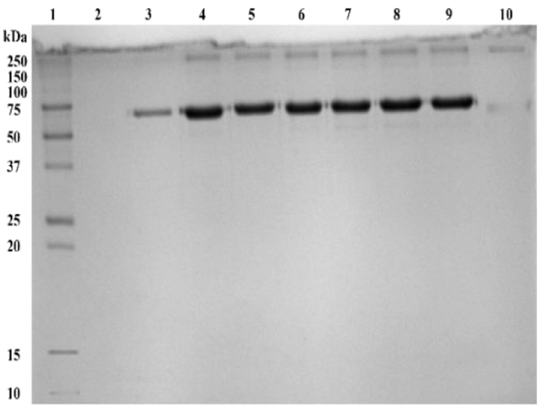

Figure 13. SDS-PAGE profile of concentration-dependent photoinduced cleavage of BSA (4 μM) exposed to UV light of 365 nm (80 W) for 30 min by complex, C_1 Lane 1, Molecular marker; Lane 2, BSA + complex (1 μM); Lane 3, BSA + complex (5 μM); Lane 4, BSA + complex (10 μM); Lane 5, BSA + complex (25 μM); Lane 6, BSA + complex (50 μM); Lane 7, BSA + complex (100 μM); Lane 8, BSA + complex (250 μM); Lane 9, BSA + complex (500 μM); Lane 10, BSA alone.

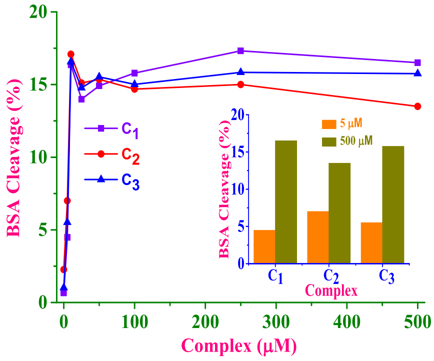

Figure 14. SDS-PAGE profile of concentration-dependent photoinduced cleavage of BSA (4 μM) exposed to UV-A light of 365 nm (84 W) for 30 min at different concentrations of the complexes by C_1, C_2, and C_3 in 50 mM Tris−HCl buffer. The inset shows a bar diagram representation of the % of BSA cleavage by each Ru−Pt complex at 5 and 500 μM.

2.6. Molecular Docking Studies. *2.6.1. Docking with B-DNA.* The molecular docking technique is an attractive scaffold to understand the metal complex−DNA interactions in rational drug design and discovery, as well as in the mechanistic study by placing a small molecule into the binding site of the target specific region of the DNA mainly in a noncovalent fashion. Molecular modeling allows for the modeling of ligand flexibility and can use more detailed molecular mechanics to calculate the energy of the ligand in the context of the putative active site. In our experiment, Ru−Pt complexes (C_1/C_2/C_3) were docked onto B-DNA to attain different conformations to predict probable binding sites and preferred orientation inside the DNA duplex of sequenced which provides an energetically favorable docked pose (lowest-energy conformations). Figure 15 shows minimum energy docked poses of C_1 (a), C_2 (b), and C_3 (c) with B-DNA duplex. The results show that complexes C_1−C_3 interact via an intercalation mode involving outside edge stacking interaction with the oxygen atom of the phosphate backbone of the DNA helix. The docked structures show that the increased planarity of the birding ligand core allows for strong π−π stacking interactions and that the complexes fit well into the intercalative in the DNA structure's G−C rich region. Planarity increased by extending the rigid π-surface on 2,3-bis(pyridyl)-pyrazinyl ligands;[23] thus C_3 has shown better binding abilities than the C_2 followed by C_1. On the other hand, as the complexes are voluminous (bulky) they may prevent

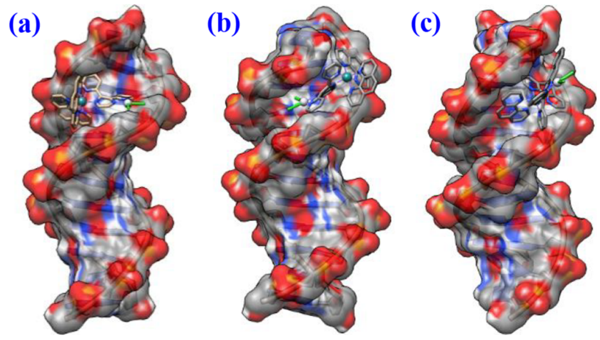

Figure 15. Docking poses, illustrating the noncovalent interactions of $\mathbf{C_1}$ (a), $\mathbf{C_2}$ (b), and $\mathbf{C_3}$ (c) with B-DNA duplex.

intercalative interaction, they are stabilized, however, by hydrogen bonding through the NH groups of the GSH moiety, whereas the complexes' interactions with DNA are dominated by noncovalent $\pi-\pi$ staking interactions. On the whole, these interactions significantly contribute to the stabilization of each Ru−Pt complex within the DNA duplex. The relative magnitude of the binding energy of complexes was found to be −29.59, −36.42, and −54.70 kJ/mol for $\mathbf{C_1}$, $\mathbf{C_2}$, and $\mathbf{C_3}$, respectively, indicating the potent binding propensity of the complexes with DNA. The computed $E_{\text{(lowest energy pose)}}$ values agree with the observed trend in binding strength from the spectroscopic (absorption and fluorescence quenching titration) and electrochemical studies (see Tables 2 and 3) with $\mathbf{C_3} > \mathbf{C_2} > \mathbf{C_1}$ as the increasing binding order. Regardless of the absence of any net positive charge on Ru−Pt complexes, a negative value of the binding energy indicated that the studied complexes had a higher binding potential with DNA. The greater the binding potency between DNA and target molecules (studied complexes), the more negative the relative binding values, which correlated well with the experimental DNA binding studies. As a result, we conclude that there is mutual coherence between spectroscopic and molecular docking techniques, which can support our experimental findings on the mode of interaction of Ru−Pt complexes with DNA and provide additional evidence of intercalative binding mode of interactions.

2.6.2. Docking with BSA.

Molecular docking was used to identify the preferential binding sites in BSA and for a better understanding of the mechanism of action for the studied Ru−Pt complexes. Serum albumin as the most abundant carrier protein comprises three a-helical homologous domains (I, II, and III), and each domain contains two subdomains (A and B). Representative Figure 16 shows the docked stable conformations of $\mathbf{C_2}$ complex into BSA, also refer to ESI Figures S18a and S18b for the docking poses of $\mathbf{C_1}$ and $\mathbf{C_3}$ with BSA, respectively. In these structures, all the complexes lie in a region of the interdomain region called protein cleft, PC paved by subdomains IA, IB, and IIA on one side and subdomains IIB, IIIA, and IIIB on the other side, mainly interacting via hydrogen bonding and van der Waals interaction.[67,68] Complex $\mathbf{C_1}$ inserts into the outer/upper PC surrounded by Lys 116 and Pro 516 residues (ESI Figure S18a), whereas $\mathbf{C_2}$ and $\mathbf{C_3}$ fit into the inner/middle PC surrounded by various kinds of hydrophobic, polar and charged residues such as Elu 189, Glu 186, Glu 182, Ile 455, Glu 399, Lys 431, Arg 427, Glu 424, Lys 114, Arg 458, Gln 403, Lys 465, Thr 518, Ser 428 (Figure 16) and Ile 455, Lys 431, Thr 518, Glu 424, Ser 428, Arg 458, Leu 189, His 145, Arg 185, Lys 114, Ala 193, Ser 192 (ESI Figure 18b), respectively. A salt bridge between Glu187 of domain I and Lys432 of domain III contributes to keeping the complexes in place. Hydrophobic and van der Waals interactions play a key role in the binding of complexes $\mathbf{C_3}$ and $\mathbf{C_2}$ at the PC_{inner} pocket, which is consistent with a thermodynamic interpretation while $\mathbf{C_1}$ interacts partially with the BSA and thus shows that the least binding interaction is in line with the experimental results. The computed binding free energies are found to be −36.94, −38.59, and −41.49 kJmol^{-1} for $\mathbf{C_1}$, $\mathbf{C_2}$, and $\mathbf{C_3}$ respectively, agreeing with the experimental ΔG values found to be −31.02, −31.55, and −31.97 kJ mol^{-1} for $\mathbf{C_1}$, $\mathbf{C_2}$, and $\mathbf{C_3}$, respectively. The relatively large negative binding energy value for the $\mathbf{C_3}$ indicates that the interactions with neighboring residues stabilize the metal complex by sturdier stronger interactions than the other two complexes and the order of binding interactions is in line with their extended π-conjugation on the bridging ring; the order is as follows: $\mathbf{C_1} < \mathbf{C_2} < \mathbf{C_3}$. Thus, the binding abilities of the studied Ru−Pt complexes well corroborate with the one obtained from thermodynamic parameter analysis.

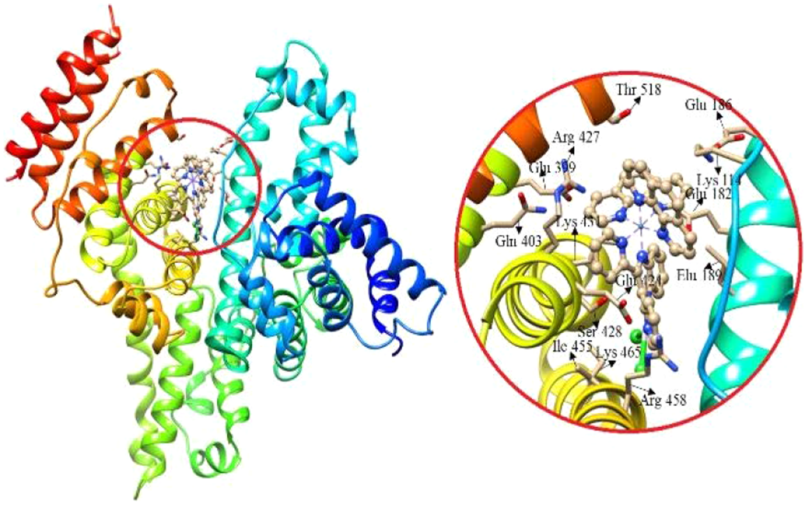

Figure 16. Lowest binding free energy conformers of the complex, $\mathbf{C_2}$ on the BSA.

2.7. In Vitro Cytotoxicity on Vero and MCF-7 Cells.

2.7.1. Cancer Cell Growth Inhibition Analysis (MTT Assay). Because we got constructive results from the CT-DNA and BSA binding interaction studies for the Ru−Pt ($\mathbf{C_1}$, $\mathbf{C_2}$, and $\mathbf{C_3}$) complexes, we have tested for their in vitro cytotoxicity ability against normal Vero and human breast adenocarcinoma, MCF-7 cell lines using the 3-(4,5-dimethylthiazol-2-yl)-2,5-diphenyltetrazoliumbromide (MTT) assay. The viability of both Vero and MCF-7 cells was compared to that of control cells after treatment with each Ru−Pt complex, and the percentage of cell viability was calculated. The cell lines were exposed to 2, 4, 8, 16, 32, and 64 M concentrations of the test complexes. Furthermore, the concentration of each complex that inhibits half (50%) of the cell growth (IC_{50} for a 24 h incubation period) value was computed and expressed in concentrations of μM. Figure 17 depicts the percentage of viable MCF-7 cells after treatment with the respective Ru−Pt complex at various concentrations. The IC_{50} values for both normal Vero and MCT-7 cell lines are tabulated in Table 5 along with cisplatin as representative data. The data showed that all three Ru−Pt complexes displayed cytotoxicity greater than 2 and 15 μM against specific MCF-7 and Vero cell lines, respectively. As a result, the studied complexes are specifically cytotoxic to MCF-7 cancer cells. However, the complexes $\mathbf{C_3}$ and $\mathbf{C_2}$ have shown higher cytotoxicity (complex $\mathbf{C_3}$ is highest) than $\mathbf{C_1}$ and also than the cisplatin against the MCF-7 cancer cell line. Moreover, the selectivity index, SI (=IC_{50} of normal cell lines/IC_{50} of cancer cell lines) of the complexes was computed, and the values for $\mathbf{C_1}$, $\mathbf{C_2}$, and $\mathbf{C_3}$ against cisplatin are 2.12, 4.38, 5.23, and 4.02, respectively (refer to Table 5). The greater the SI value (>2), the higher the selective toxicity toward cancer cells while a smaller SI value (<2) is considered to give indiscriminate toxicity which can also cause cytotoxicity in normal cells. These higher SI values of 5.23 (for $\mathbf{C_3}$) and 4.02 (for $\mathbf{C_2}$) emphasize that the two complexes are more cytotoxic and selective against MCF7 cell lines than cisplatin. This agrees with the reactivity trend ($\mathbf{C_1} < \mathbf{C_2} < \mathbf{C_3}$) with studied nucleophiles which implies that $\mathbf{C_3}$ is likely to react fastest with the DNA due to the increase in extended π-conjugation on the 2,3-bis(pyridyl)pyrazinyl bridge ligand moiety. The higher cytotoxicity and selectivity for complexes $\mathbf{C_3}$ and $\mathbf{C_2}$ than cisplatin imply a favorable synergetic effect by Pt−Ru coordination sites. These two complexes could be considered for further development to attain more dynamic and selective chemotherapeutic agents against breast cancer cells.

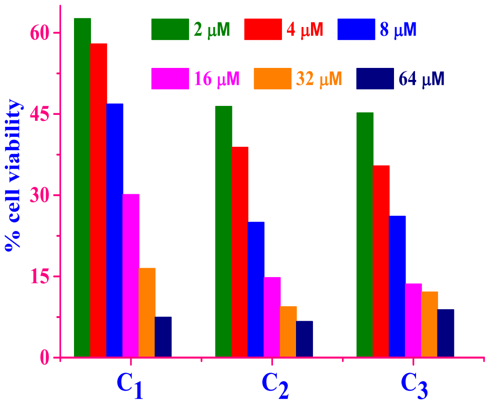

Figure 17. Percentage of cell viability of MCF-7 (b) cells when treated with different concentrations of each of Ru−Pt complex for 24 h.

Table 5. IC_{50} (μM) Values of the Tested Ru−Pt Complexes toward the Normal Vero and Selected Breast Cancer MCF-7 Cell Lines[a]

complex	normal Vero	breast cancer MCF-7	SI[b]
$\mathbf{C_1}$	19.3 ± 2.1	9.1 ± 1.5	2.12
$\mathbf{C_2}$	17.5 ± 1.9	4.0 ± 1.1	4.38
$\mathbf{C_3}$	16.2 ± 1.7	3.1 ± 0.8	5.23
cisplatin	20.1 ± 2.4[69]	5.0 ± 1.1[70]	4.02

[a] Data are calculated by mean ± standard deviation (SD) of three independent experiments, i.e., $n = 3$, for 24 h of incubation. [b] IC_{50} of Vero cell line/IC_{50} of MCF-7 cell line.

2.7.2. Apoptotic Analysis by Acridine Orange/Ethidium Bromide (AO/EB) Staining Assay. Morphological changes due to apoptosis caused by the Ru−Pt complexes obtained using fluorescence microscopic analysis were studied by performing the differential staining technique using AO/EB. AO can pervade intact cell membranes and stain the nuclei green in color, whereas EB can only stain the nuclei of cells that have lost membrane integrity.[71] The MCF-7 cells were separately exposed for 24 h to the three different Ru−Pt complexes at a concentration of 10 μM, and the morphological changes after the AO-EB staining process were pictured. Figure 18 compares the AO/EB staining assay images of MCF-7 cancer cell lines treated for 24 h with a fixed concentration of 10 M of each complex, $\mathbf{C_1}$ (b), $\mathbf{C_2}$ (c), and $\mathbf{C_3}$ (d), to the control (a). It is inferred that the morphology of the control (untreated) MCF-7 cancer cells remains intact, stained as green fluorescence images indicating the cell viability. On the contrary, the cells treated with a fixed dose of 10 μM of each Ru−Pt complex clearly revealed significant morphological changes as they stained as yellow colored fluorescence images. Thus, these complexes induce early apoptotic cell damage characterized by membrane blebbing. The orange color fluorescence stained images are certainly owing to cells in their late apoptotic induced changes. The stains appear as dense spots because of the formation of highly condensed chromatin due to its aggregation. The bright red color fluorescence stain image is

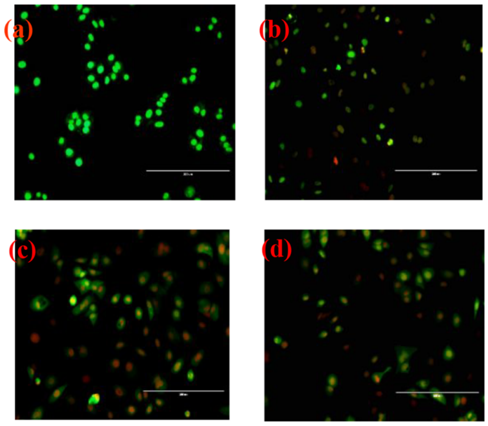

Figure 18. AO/EB staining assay images of the MCF-7 cancer cell lines treated with a fixed concentration of 10 μM of each Ru−Pt complex ($\mathbf{C_1}$, b; $\mathbf{C_2}$, c; $\mathbf{C_3}$, d) for 24 h and compared with the control (a).

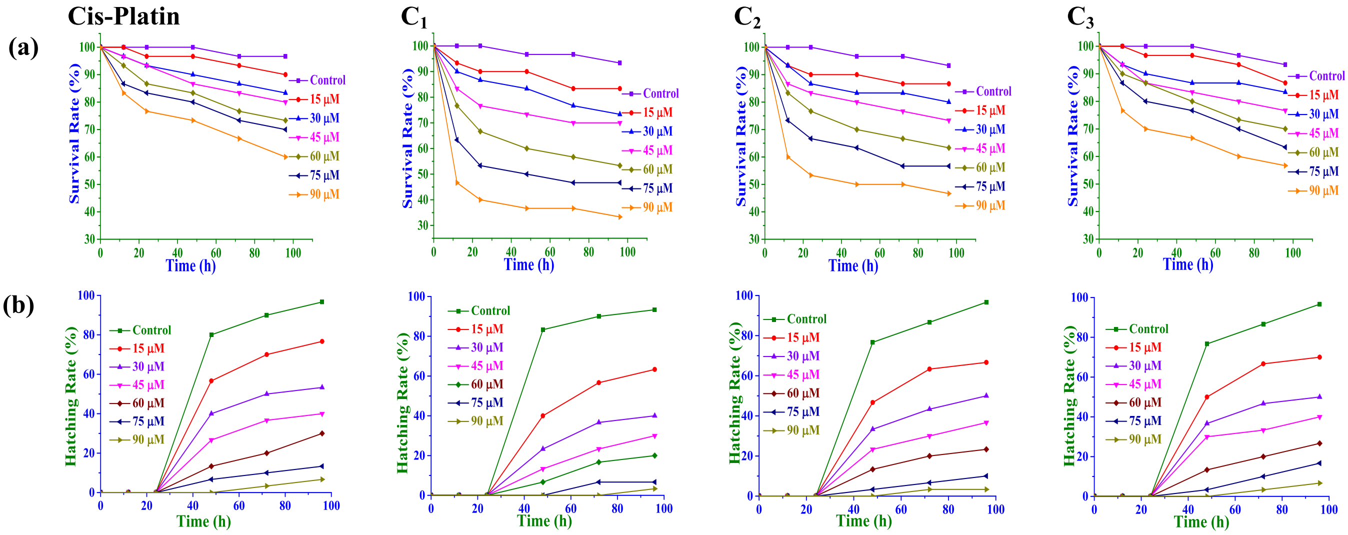

Figure 19. Survival (a) and hatching (b) rates of zebrafish embryos treated with cisplatin and each Ru−Pt complex at 0−96 hpf. Data collected from 10 embryos per well condition and three replicates of three independent trials.

due to cells that have been necrosis, significantly indicating the typical dead cells. The color changes signify an early induction of the apoptosis stage as well as a nuclear condensation effect of the cells by the cytotoxic Ru−Pt compounds. These are the typical features of apoptotic cells and are quite dissimilar from those of the control cells. Overall, the findings show that necrosis of MCF-7 cells occurred at a significantly lower dose of Ru−Pt complexes (10 M). This is consistent with their high in vitro cytotoxicity as determined by the MTT assay. This suggests that the Ru−Pt complexes caused early apoptosis in the MCF-7 cancer cell line, which is not toxic to normal Vero cells.

2.8. In Vivo Toxicity Assessment Using Zebrafish Embryos. In recent years, the development of zebrafish embryos has become a prominent high-quality in vivo validation model for drug discovery and toxicology evaluations because of their rapid embryogenesis, small size, short reproductive cycle, high transparency, low cost-effectiveness, and most importantly their high degree of genetic conservation with mammals.[72,73] Thus, the zebrafish embryo acute toxicology (FET) test is a substitute method for premammalian studies to reduce/replace mammalian vertebrate usage and assess the toxicity in a short time. Cisplatin was accepted as a reference material by the Food and Drug Administration in 1978 despite some dose-limiting side effects; hence, the data on cisplatin toxicology in zebrafish emerged as a model.[74]

The FET test was tested by treating the live zebrafish embryos (4 cell stage and 10 embryos per well) with increasing concentrations (0.0−90.0 μM with 15 μM increments) of the Ru−Pt complexes (**C$_1$**, **C$_2$**, and **C$_3$**) and cisplatin. In the negative control (without treatment of any compound), almost all of the zebrafish embryos survived and developed into full juvenile zebrafish. However, the solvent control was relatively toxic at 120 h postfertilization, hpf compared to the negative control; thus, treatments were limited only for up to 96 hpf. It is found that the mortality rates of embryos in the solvent control were similar to those of the negative control-treated embryos. The % of survival and hatching rates data are given in ESI Tables S8 and S9, respectively, and the data are depicted in Figure 19. Representative images of zebrafish embryos at the 96 h after treatment with cisplatin and each Ru−Pt complex at 15 and 90 μM are shown in Figure 20. Toxicological estimates show an LC$_{50}$ (a dose that leads to 50% death of the embryos and the data expressed as mean ± SD from three replicates of three independent experiments) of 181.1 ± 2.1, 65.2 ± 1.0, 96.3 ± 1.4, and 148.8 ± 1.7 μM for cisplatin, **C$_1$**, **C$_2$**, and **C$_3$**, respectively and the toxicity increases from **C$_1$** to **C$_3$** as the extended π-conjugation increases on the backbone of the ligand.

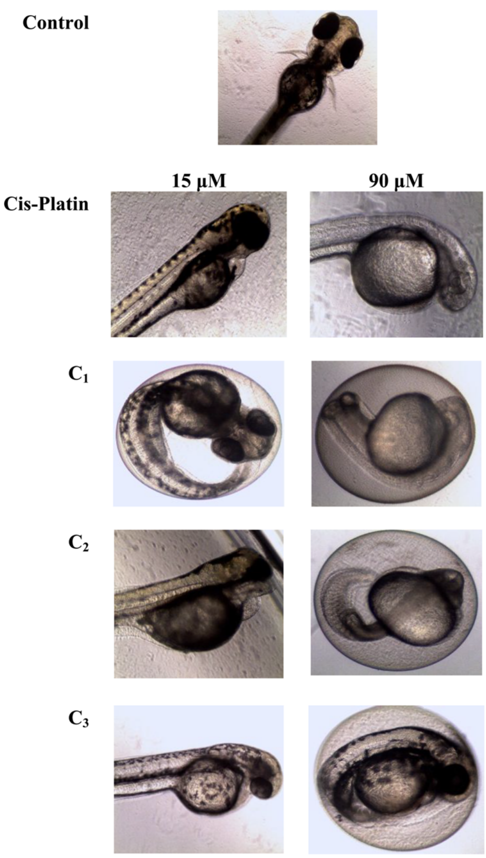

Figure 20. Representative images of zebrafish embryos treated with cisplatin and each Ru−Pt complex at 15 and 90 μM at 96 hpf.

After 96 hpf of treatment, the survival rate was over 90% when the concentration of cisplatin is 15 μM or lower and the value drops to 60% when 90 μM, results are comparable to the literature.[75] In a comparison of cisplatin, the **C_3** complex shows comparable survival rates at all the concentrations (86.7 and 56.7% at 15 and 90 μM, at 96 h, respectively, refer ESI Table S8 and Figure 19a). The survival rate dropped to 50% for **C_1** while it was limited to 30% in **C_3** when the concentration increased from 15 to 90 μM, indicating that the latter complex is less toxic as it reflected its LC_{50} value.

Hatching success is thought to be a sensitive endpoint of the zebrafish embryo in toxicity assays because no hatched embryos died.[76] In terms of hatching rate, it was discovered that the studied complexes caused a 48-hour delay in the hatching. When the concentration is increased to 90 M, only about 6.7% of embryos can develop into juvenile zebrafish for both **C_3** and cisplatin compared to the negative control, and the percentage decreased gradually from **C_3** to **C_1** (see Figure 9b and ESI Table S9). Overly, about 25% of embryos are abnormal and have difficulty growing into juvenile zebrafish with 45 μM or higher concentration of **C_3** which is similar to cisplatin. The data confirm that these complexes slow down the development/hatching of embryos to juvenile zebrafish. However, all survived embryos were hatched later and reached about 100% and there were no statistical changes between the treated and the negative control. A literature survey revealed that the treatment with cisplatin appeared to be nontoxic in developing zebrafish embryos, even under 15 μM while inducing delayed hatching up to 120 hpf.[77] However, it significantly induced a lethal outcome even at a higher concentration of 400 μM[78] which is in accordance with the current results.

The morphological investigations of the embryos revealed that the cisplatin and Ru−Pt complexes (**C_1**, **C_2**, and **C_3**) did not induce any significant morphological changes in zebrafish embryos, even at 90 M of the three complexes (see Figure 18). The treated embryos' ocular and corporal pigmentation, somite formation, tail detachment, heartbeat, and blood circulation showed no significant differences from the negative control. Thus, these findings show that the studied Ru−Pt complexes did not induce embryotoxicity or toxicity in the development of zebrafish embryos and larval to juvenile zebrafish at any of the six concentrations tested. However, data on the survival rates for the 96 hpf period showed that **C_1** and **C_2** were relatively more toxic to the zebrafish embryos than **C_3**. Moreover, the toxicity effects were concentration-dependent on each Ru−Pt complex used for treatment. These findings suggest that C3 is less toxic to zebrafish embryos, with the decreasing toxicity order being **C_1** > **C_2** > **C_3** ≈ cisplatin. We concluded that the complexes do not exhibit significant signs of lethal toxicity even at 90 M concentrations, supporting the idea that the studied Ru−Pt complexes are promising antitumor agents.

3. CONCLUSIONS

The reactivity toward the substitution three of Ru−Pt heterodinuclear complexes was found to be **C_1** < **C_2** < **C_3** and correlated well with the size of the π-surface and hence the extended π-back bonding into the 2,3-bis(pyridyl)pyrazinyl ligands. The rate of chloride substitution depends on the donor atom on the incoming nucleophiles. S-donor Tu has shown the highest reactivity because it is a very good π/σ-donor, moreover a sterically less demanding molecule while the N-donor 5′-GMP nucleophile showed the least reactivity owing to its crowded size which causes more steric hindrance with the complex. Thus, the decreasing reactivity order of the studied nucleophiles follows Tu > L-Met >5′-GMP. The dechelation of ligands on the Pt(II) end of the complexes was noticed only for the reactions with Tu due to its strong trans effect, whereas for the L-Met and 5′-GMP reactions, S, N-chelation and bulkiness of the ligand prevent the dechelation of Pt(II), respectively.

The binding experiments with CT-DNA and BSA revealed that the complexes interact strongly via the intercalative binding mode and the binding order corresponds to their reactivity. Photoinduced cleavage experiments with pcDNA/BSA revealed that all three Ru−Pt complexes cleavage DNA by more than 24% for all three complexes, whereas the complex, **C_3** has shown least of 17% at 250 μM while the BSA cleaved about 20% at 500 μM. This suggests that all three complexes have similar photoinduced BSA cleavage activity. The cleavage abilities are inversely correlated with their binding abilities, which support their order of interactions with DNA/BSA. Molecular docking simulation results show DNA helix nursing the intercalative mode of interaction of complexes **C_1−C_3** and the binding strength increases with the planarity of birding ligand core which is comfortable for strong $\pi-\pi$ stacking interactions. Furthermore, studies with BSA showed that excellent binding affinity of these complexes lies in a interdomain region called protein cleft, via hydrogen bonding and van der Waals interaction.

In vitro MTT cytotoxic activities of the complexes revealed good cytotoxicity activity toward the human breast cancer cell line MCF-7 and the least effect on normal Vero cell lines. The complex **C_3** showed the highest cytotoxicity (IC_{50} = 3.1 μM) and selectivity (5.55) than the commercial cisplatin (IC_{50} and SI values are 5.0 μM and 4.02, respectively). The fluorescence AO/EB staining assay revealed morphological changes which are suggestive of early apoptotic induction, as well as nonspecific necrosis, which appeared to involve autophagy of the MCF-7 cells occurred at a significantly lower dose (10 μM) of the Ru−Pt complexes. This is in good agreement with their high in vitro cytotoxicity obtained by the MTT assay. While the Ru−Pt complexes prompted early apoptosis in the MCF-7 cancer cell line, they were nontoxic to the normal Vero cells. In vivo FET toxicological assessment on zebrafish embryos revealed toxicity (LC_{50} > 65.2 μM) effects during embryonic and larval development over 96 hpf. However, **C_3** has toxicity (148.8 μM) which is similar to that of cisplatin (181.1 μM) at higher concentrations of 90 μM. Thus, complex **C_3** is a relevant antitumor metallodrug candidate for promising more effective drugs for MCF-7 breast cancer treatment and the least toxicity against zebrafish embryos. Therefore, we report that these heterodinuclear Ru−Pt complexes defeat cancer metastasis also to have significantly enhanced cancer cell selectivity and reduced in vivo toxicity.

4. EXPERIMENTAL SECTION

4.1. Reagents, Materials, and Instrumentation.

Sigma-Aldrich provided all of the reagents, which were used without further purification. According to the literature, ligand precursors, intermediate complexes, and corresponding dichloro Ru−Pt complexes were synthesized, and the results were reported.[23]

4.1.1. 2,3-Bis(2′pyriyl)-quinoxaline, bpq. A one-hour reflux of an equimolar mixture of 2,2′-pyridil and *O*-phenylenediamine solutions in ethanol was filtered (while still hot) to remove unreacted starting materials, yielding a light brown product on cooling. The product was collected using Millipore filtration and recrystallized from hot ethanol.

4.1.2. 2,3-Bis(2′pyriyl)benzo[g]quinoxaline, bbq. An equimolar mixture of ethanol solutions of 2,2′-pyridil and 2,3-diaminonaphthalene was refluxed for 1 h under constant stirring. Rotary evaporation and filtering were used to reduce the volume to half. After cooling the filtrate for 48 h, a crystalline product was separated. The product was filtered and recrystallized from hot ethanol.

4.1.2.1. Synthesis of Ru(II) Precursor, (phen)$_2$RuCl$_2$. In 50 mL of dimethyl formamide, a 1:2 mole ratio of ruthenium(*III*)chloride trihydrate and 1,10-phenanthroline was dissolved, along with 0.5 mmol of lithium chloride, and refluxed for about 8 h with constant stirring. After the reaction mixture has cooled to room temperature, 250 mL of acetone was added and in a freezer at −5 °C for 24 h. Suction was used to collect the microcrystalline dark green precipitate, which was then washed several times with aliquots of ice water and diethyl ether before drying under a vacuum.

4.1.2.2. Synthesis of (phen)$_2$Ru(bpp/bpq/bbq)(PF$_6$)$_2$. A 100 mL ethanolic solution of equimolar (phen)$_2$RuCl$_2$ and **bpp**/ or **bpq**/ or **bbq** was refluxed for hours with constant stirring, and the reaction mixture was filtered while it was still hot. Reddish brown powder(s) were precipitated when an aqueous KPF$_6$ solution was added to the chilled filtrate(s). The products were collected using suction, then washed with water and diethyl ether, vacuum-dried, and recrystallized from a 1:1 water–ethanol solution.

*4.1.2.3. Synthesis of (phen)$_2$Ru(μ-bpp/bpq/bbq)-PtCl$_2$(PF$_6$)$_2$, **C$_1$/C$_2$/C$_3$**.* A suspension of 1:2 molar ratio of (phen)$_2$Ru(bpp)(PF$_6$)$_2$ or (phen)$_2$Ru(bpp)(PF$_6$)$_2$ or (phen)$_2$Ru(bpp)(PF$_6$)$_2$, PtCl$_2$(DMSO)$_2$ in 50 mL of ethanol was refluxed for 48 h under a nitrogen gas flow. After filtering out unreacted starting materials, the cooled filtrate was treated with a saturated solution of KPF$_6$ to induce precipitation. Vacuum filtration was used to collect the microcrystalline precipitate(s). The powders were redissolved in acetonitrile and precipitated by slowly adding 200 mL of chilled diethyl ether. Filtration was used to collect the purified precipitates, which were then washed with aliquots of water and diethyl ether and dried under vacuum.

Kinetic measurements were taken using a Varian Cary 100 Bio UV–visible spectrophotometer connected to a Varian Peltier temperature controller with a 0.05 °C accuracy. The ESI data show how to prepare Ru–Pt complexes and nucleophiles for kinetics, as well as the kinetic procedure used to calculate rate data.

4.2. Stability of the Complexes. The complexes were soluble in DMF and DMSO, moderately soluble in water and alcohols, and less soluble in MeCN and CH$_2$Cl$_2$ solvents. They were stable in the solid and solution phases. Thus, concentrated 5 mM stock solutions of each Ru–Pt complex were dissolved in 5% DMF/DMSO for kinetics/biological studies, respectively, followed by appropriate dilutions with buffer pH 7.2 (5 mM Tris–HCl/50 mM NaCl buffer) to obtain the desired complex concentration in the final volume of samples. All stock solutions were prepared, and dilutions were carried out immediately before sample preparation. Individual samples were prepared and incubated overnight (about 14 h) at 37 ± 1 °C to ensure that equilibrium was fully attained before measurements.

4.3. CT-DNA Binding Studies. *4.3.1. Absorption Spectral Studies.* The ability of Ru–Pt complexes to bind to CT-DNA can provide simulation data that can be used to better understand their anticancer mechanism of action in biological systems.[79] Aside from covalent binding, metal complexes interact with DNA via electrostatic associative binding, groove formation, or intercalation between base pairs.[80] One of the most widely used techniques for determining the binding abilities of complexes with duplex DNA helix is absorption spectroscopy. Absorption bands between 260 and 400 nm are typically attributed to intraligand charge transfer transitions of type $\pi \rightarrow \pi^*$ and $n \rightarrow \pi^*$, whereas bands above 350 nm are attributed to ligand-to-metal and metal-to-ligand charge transfers (LMCT and MLCT bands).[81] Thus, the spectral changes in the MLCT/LMCT bands caused by the addition of DNA can be used to characterize direct interactions between metal complexes and DNA. The ESI data contain all of the details pertaining to the solution preparation, experimental method, and computation of the binding constant.

4.3.2. Fluorescence Spectral Studies. Because the investigated Ru–Pt complexes (**C$_1$**, **C$_2$**, and **C$_3$**) do not fluoresce at room temperature in the presence of CT-DNA, the complexes' CT-DNA binding abilities were deduced indirectly from their ability to quench the emission of CT-DNA–EtBr solution. EtBr is a planar cationic dye that intercalates with DNA to form soluble and highly fluorescent complexes with nucleic acids. However, no significant fluorescence emission is observed in the Tris–HCl buffer. However, due to the extraneous rigidity of its immediate environment in the solution phase, its DNA intercalating complex fluorescence intensity λ_{em} is approximately equal to 600 nm.[82] The competitive binding studies were thus carried out by monitoring the quenching of the fluorescence emission intensity of the EtBr-DNA complex after each addition of the Ru–Pt complex. The ESI data contain a detailed methodology for calculating the binding data.

4.4. BSA Binding Studies. *4.4.1. Absorption Spectral Studies.* UV–visible spectroscopy is the simplest method for determining the type of quenching (static or dynamic) of BSA fluorescence intensities in fluorescence spectral studies with each metal complex. Static quenching refers to the formation of a complex adduct of fluorophore and quencher in the ground state, whereas dynamic quenching occurs when the fluorophore and quencher come into contact with each other during the excited state's transient existence.[83] The interactions between BSA and the studied complexes are revealed by using a fixed concentration of BSA (20 M) and BSA with each Ru–Pt complex. The enhancement with a prominent blue shift and the diminution with a prominent red shift in the absorption intensity of BSA with the addition of each complex with reference to the BSA absorption intensity indicates that the quencher (metal complexes) quenches the fluorescence intensities of BSA static and dynamic, respectively.

4.4.2. Fluorescence Spectral Studies. The method for quenching BSA fluorescence emission by complexes (**C$_1$**, **C$_2$**, and **C$_3$**) is essentially the same as for CT-DNA + EtBr quenching. The detailed procedure, on the other hand, was provided in ESI data.

4.5. Filter Effect Corrections. The filter effect, which consists of the absorption of exciting and/or emitted radiation by dissolved species, including the fluorophore itself, occurs as the fluorophore concentration in the solution increases continuously.[84] To evaluate existing primary and/or secondary inner filter effects, a Shimadzu UV-1800 UV−visible spectrophotometer was used (IFEs). The fluorescence intensities were measured using 510/280 (CT-DNA/BSA) and 597/347 nm excitation and emission wavelengths, respectively. To eliminate the possibility of reabsorption and the inner filter effect due to UV−Visible absorption of each Ru−Pt complex, (**C**$_1$, **C**$_2$, and **C**$_3$) the fluorescence data of CT-DNA/BSA were corrected for excitation and emitted light absorption according to eq 4.[85]

$$F_{corr} = F_{obs}10^{(A_{ex}+A_{em})/2} \tag{4}$$

where F_{corr} and F_{obs} are the corrected and observed fluorescence intensities, respectively, caused by quencher/fluorophore addition in a 1 cm path-length cuvette. This straightforward equation was chosen because it is valid and applicable in the case of typical fluorophores where scattering is negligible and absorption dominates extinction.

4.6. Viscosity Measurements. The viscosity was measured with an Ubbelodhe viscometer immersed in a thermostatic water bath at 25 (± 0.1) °C. To reduce the complexity caused by DNA flexibility, CT-DNA samples were prepared using sonication. A constant concentration of (5.0 mM) CT-DNA was treated with varying amounts of each complex. After 15 min equilibrium, the flow time of samples was measured in triplicate using a digital stopwatch to obtain the concurrent values. The relative viscosities for CT-DNA in the presence and absence of the Ru−Pt complexes or EtBr were calculated from the relation $\eta = (t - t_0)/t_0$, where t is the observed flow time of CT-DNA containing Ru−Pt complex or EtBr and t_0 is the flow time of Tris−HCl buffer alone. Data are presented as $(\eta/\eta_0)^{1/3}$ versus binding ratio, where η is the viscosity of CT-DNA in the presence of Ru−Pt complex/EtBr and η_0 is the viscosity of CT-DNA alone.

4.7. Cleavage Studies. *4.7.1. DNA Cleavage Studies.* Agarose gel electrophoresis is a versatile technique for monitoring DNA cleavage activity induced in the presence of each studied Ru−Pt complex by observing changes in DNA mobility when an electric field is applied. In ESI data, full details of the gel's preparation, metal solutions, and the reagents/instruments used to run the gel, as well as their final band images, are provided.

4.7.2. BSA Cleavage Studies. The BSA photoinduced cleavage activity of the compounds was studied using BSA (4 M) in Tris−HCl buffer (50 mM, pH 6.8) with SDS-PAGE (sodium dodecyl sulfate-polyacrylamide gel electrophoresis) at 27 °C according to the literature.[86] Refer to ESI data for the complete description of staking/running gel preparation and other details.

4.8. In Silico Docking Simulations. For rational drug design, molecular docking was used to study the binding mode and intermolecular interactions of the Ru−Pt complexes (**C**$_1$, **C**$_2$, and **C**$_3$) with DNA and BSA using the online servers PatchDock and FireDock, with the high-quality three-dimensional optimized conformers of the complexes used as the ligands during each calculation. The ESI data contain a detailed description of the docking procedures for both DNA and BSA, as well as additional information.

4.9. In Vitro Cytotoxicity Studies. The normal Vero and human breast adenocarcinoma (MCF-7) cell lines were obtained from the National Centre for Cell Sciences Repository at the University of Pune in India. Vero and MCF-7 cells were grown in minimal essential medium and Dulbecco's modified Eagle's medium, respectively, supplemented with (v/v) 10% fetal bovine serum, 100 g/mL penicillin, and 100 g/mL streptomycin. The cells were incubated for 48 h in a humidified atmosphere at 37 °C with 5% CO_2. Detailed cell culture and protocols followed to investigate cytotoxicities of the Ru−Pt complexes by MTT and AO-EB assay are given in ESI data.

4.10. In Vivo Toxicity Assessment Using Zebrafish Embryos. Adult zebrafish (*Danio rerio*, Wild Type) were kept in an aquaria system with a closed circuit of water under controlled physicochemical conditions such as temperature, pH, hardness, conductivity, and ammonia over a 14-hour light/10-hour dark cycle.[87] Feeding occurred three times per day; more information can be found in the ESI data. Adult males and females were kept apart until the night before the massive spawning event. After the lights were turned on the next day, eggs were collected from breeders. Immediately after spawning, eggs were rinsed with sterile dechlorinated tap water, and fecundity was confirmed by visual inspection, discarding those that were not fertilized or malformed. The embryos were then exposed to various treatments as soon as possible, with three replicates of 10 embryos transferred individually to 24-well plates containing 250 L of the evaluated compounds dissolved in embryo medium[87] which contained (in mM) 0.5 NaCl, 0.2 CaSO4, 0.2 MgSO4, 0.16 KH_2PO_4, and 0.16 K_2HPO_4 (adjust pH to 7.2 using HCl) in double-distilled water. Cisplatin and each Ru−Pt complex (**C**$_1$−**C**$_3$) were diluted into the embryonic media, and aliquots of 200 μL were prepared at six different concentrations of each complex starting from 15 and finishing at 90 μM (geometric series of 15 90 μM). The screening medium contains DMSO used to solubilize the complexes that did not exceed 0.5% v/v in final solutions. A negative control (embryos medium) and a positive/solvent control (embryos medium with <0.5% DMSO) were monitored to ascertain the effect of the solvent. Embryos were maintained in an incubator at 26.8 ± 1 °C. Lethal endpoints on zebrafish embryos were evaluated: the number of coagulated embryos, lack of somite formation (suggesting general developmental retardation), the nondetachment of the tail, and absence of heartbeat (visible after 48 h postfertilization, hpf in normal developing embryos), and measured characteristic morphological changes are tabulated in ESI Table S10. The heartbeat was evaluated by monitoring blood circulation in the yolk. Also, the hatching time was recorded to investigate the effects of retardation on embryo development. All these significant effects on the embryos by treating with cisplatin and studied Ru−Pt complexes in comparison to the control were recorded every 24 hpf from the beginning of the experiment up to 96 hpf at different concentrations. Individual embryo surviving larvae were assessed under a stereomicroscope (SMZ-1500, Nikon, Japan). Care, use, and treatment of zebrafish were done under the procedures approved by competent authorities and European Community Guidelines on Animal Care and Experimentation which is approved by the animal care and use committees.

4.11. Statistical Analysis. The EFT tests followed all survival/mortality rates necessary to be valid. Mortality data after 96 hpf of chemical exposure from toxicity assessment were analyzed for determining the LC_{50} values (LC_{50} is the dose that leads to 50% death of the embryos, expressed in μM). Each embryo was examined, and the statistical analysis was made using Regression Probit analysis.[88] The survival/mortality data were corrected taking into account control mortality with Abbott's formula.[89] Data are expressed as the standard error of the mean of triplicates of three individual experiments.

■ ASSOCIATED CONTENT

SI Supporting Information

The Supporting Information is available free of charge at https://pubs.acs.org/doi/10.1021/acsomega.2c01845.

Figure S1: UV-Vis spectral changes for the reaction between 50 μM of **C2**/**C3** and Tu (40-fold excess); Figure S2: Plots of *k*obs on [L-Met] for the first step for the reaction between Ru-Pt complexes with L-Met: [**C1**/**C2**/**C3**] = 50 μM and pH = 7.2 (5.0 mM Tris-HCl and 50 mM NaCl); Figure S3: Plots of *k*obs on [5-GMP] for both first and second steps for the reaction between Ru-Pt complexes with 5-GMP: [**C1**/**C2**/**C3**] = 50 μM and pH = 7.2 (5.0mM Tris-HCl and 50 mM NaCl); Figure S4: Plots of *k*obs versus [Nu] for both first and second steps for the reaction between complex **C2** with Nu: [**C2**] = 50 μM and pH = 7.2 (5.0 mM Tris-HCl and 50 mM NaCl); Figure S5: Plots of *k*obs versus [Nu] for both first and second steps for the reaction between complex **C3** with Nu: [**C3**] = 50 μM and pH = 7.2 (5.0 mM Tris-HCl and 50 mM NaCl); Figure S6: Eyring plots for the first step for the reaction between Ru-Pt complexes with Tu and L-Met and 5'-GMP ; Figure S7: Eyring plots for the second step for the reaction between Ru-Pt complexes with Tu and L-Met and 5'-GMP ; Figure S8: *Iso*-kinetic plot for the first step of the reactions of all the three Ru-Pt complexes with Nus; Figure S9: ORTEP view and atom numbering scheme of the Pt(Tu)4.2NH2(CH3)2.ClO4.Cl complex with displacement ellipsoid at 50 % probability; Figure S10: Absorption spectra of 14 μM **C2** and **C3** in Tris-HCl/50 mM NalCl buffer at pH 7.2 upon addition of CT-DNA (0−90 μM); Figure S11: Fluorescence emission spectra of EtBr bounded to CT-DNA in the presence of **C2**; Figure S12: Fluorescence emission spectra of EtBr bounded to CT-DNA in the presence of **C3**: [EtBr] = 20.0 μM, [CT-DNA] = 20.0 μM and [**C3**] = 0−150 μM; Figure S13: Effect of increasing amounts of **C1**, **C2**, **C3** and EtBr on the relative viscosities of CTDNA in 5 mM Tris-HCl/50 mM NaCl, pH 7.2; Figure S14: Absorption spectra of 10 μM BSA with and without 5 μM of each Ru-Pt complex; Figure S15: Fluorescence emission spectra of BSA in the absence and presence of **C2**: [BSA] = 1.08 μM and [**C2**] = 0−20 μM; Figure S16: Fluorescence emission spectra of BSA in the absence and presence of **C3**: [BSA] = 1.08 μM and [**C2**] = 0−20 μM; Figure S17: SDS-PAGE profile of concentration dependent photo-induced cleavage of BSA (4 μM) in UV light of 350 nm (80 W) for 30 min by complex; Figure S18: The lowest binding free energy conformers of **C1** and **C3** with BSA; Table S1: Summary of the second order rate constants, *k*2 for the first steps of the Ru-Pt complexes with Nu at 25, 45, and 55 °C; Table S2: Summary of the rate constants for the second steps of the Ru-Pt complexes with Nu at 25, 45, and 55 °C (* $k1^{2nd} \times 10^4$, s^{-1}); Table S3: Activation parameters for the both first and second steps of the reaction between Ru-Pt and Nus; Table S4: Crystallographic data and structure refinement details for complex **Pt(Tu)4**; Table S5: UV-Vis titration data between Ru-Pt complexes (**C1**−**C3**) with CT-DNA; Table S6: Spectro flurometric titration data between Ru-Pt complexes (**C1**−**C3**) with CT-DNA; Table S7: The percentage of 0.1 μM pcDNA cleavage at concentration gradient of Ru-Pt complexes; Table S8: Survival rates of zebrafish embryos assessments after the exposure of cis-platin and each Ru-Pt complex using zebrafish embryos; Table S9: Hatching rates of zebrafish embryos assessments after the exposure of cis-platin and each Ru-Pt complex using zebrafish embryos; Table S10: Morphological characteristics evaluated as measures of the Ru-Pt complexes at the designated time points; Solutions and kinetic procedure; binding studies; cleavage studies; *in silico* docking simulations; *in vitro* cytotoxicity studies; *in vivo* zebrafish embryo toxicity studies (PDF)

■ AUTHOR INFORMATION

Corresponding Author

Rajesh Bellam − *School of Chemistry and Physics, University of KwaZulu-Natal, Scottsville 3209 Pietermaritzburg, South Africa; Reseda Lifesciences Pvt. Ltd., Bangalore 560041 Karnataka, India;* orcid.org/0000-0001-9009-0211; Email: rajeshchowdarybellam@gmail.com

Authors

Deogratius Jaganyi − *School of Pure and Applied Sciences, Mount Kenya University, Thika, Kenya; Department of Chemistry, Durban University of Technology, Durban 4000, South Africa*

Ross Stuart Robinson − *School of Chemistry and Physics, University of KwaZulu-Natal, Scottsville 3209 Pietermaritzburg, South Africa*

Complete contact information is available at: https://pubs.acs.org/10.1021/acsomega.2c01845

Notes

The authors declare no competing financial interest.

■ ACKNOWLEDGMENTS

We acknowledge financial support from the University of KwaZulu-Natal, South Africa as a Postdoctoral fellowship to Dr. Rajesh Bellam. Thanks are extended to Prof. Raymond Hewer, for providing facilities to conduct the FET test and their assistance during the optimization and analyzing results.

■ ABBREVIATIONS

bpp, 2,3-bis(2-pyridyl)pyrazine
bpq, 2,3-bis(2-pyridyl)quinoxaline
bbq, 2,3-bis(2-pyridyl)benzo[*g*]quinoxaline
C_1, [(1,10-phenanthroline)$_2$Ru(II)(μ-2,3-bis(2-pyridyl)-pyrazine)Pt(*II*)dichloride]$^{2+}$
C_2, [(1,10-phenanthroline)$_2$Ru(II)(μ-2,3-bis(2-pyridyl)-quinoxaline)Pt(*II*)dichloride]$^{2+}$
C_3, [(1,10-phenanthroline)$_2$Ru(II)(μ-2,3-bis(2-pyridyl)-benzo[*g*]quinoxaline)Pt(*II*)dichloride]$^{2+}$
Tu, thiourea
L-Met, L-methionine
5′-GMP, guanosine-5′-monophosphate
CT-DNA, calf thymus deoxyribonucleic acid
EtBr, ethidium bromide

MTT, 3-(4,5-dimethylthiazol-2-yl)-2,5-diphenyl tetrazolium bromide
AO/EB, acridine orange/ethidium bromide
IC$_{50}$, half-maximal inhibitory concentration
Lc$_{50}$, lethal concentration 50
FET, zebrafish embryo acute toxicology

■ REFERENCES

(1) Jamieson, E. R.; Stephen, J. L. Structure, recognition, and processing of cisplatin− DNA adducts. *Chem. Rev.* **1999**, *99*, 2467−2498.

(2) Han, X.; Xiaolian, G. Sequence specific recognition of ligand-DNA complexes studied by NMR. *Curr. Med. Chem.* **2000**, *8*, 551−581.

(3) Demirci, S.; Doğan, A.; Başak, N.; Telci, D.; Dede, B.; Orhan, C.; Tuzcu, M.; Şahin, K.; Şahin, N.; Özercan, I. H.; Şahin, F. A Schiff base derivative for effective treatment of diethylnitrosamine-induced liver cancer in vivo. *Anti-Cancer Drugs* **2015**, *26*, 555−564.

(4) Reedijk, J. Why does cisplatin reach guanine-N7 with competing S-donor ligands available in the cell? *Chem. Rev.* **1999**, *99*, 2499−2510.

(5) Topală, T.; Bodoki, A.; Oprean, L.; Oprean, R. Bovine serum albumin interactions with metal complexes. *Clujul Med.* **2014**, *87*, 215.

(6) Rosenberg, B.; Van Camp, L.; Krigas, T. Inhibition of cell division in Escherichia coli by electrolysis products from a platinum electrode. *Nature* **1965**, *205*, 698−699.

(7) Kelland, L. The resurgence of platinum-based cancer chemotherapy. *Nat. Rev. Cancer* **2007**, *7*, 573−584.

(8) Wong, E.; Giandomenico, C. M. Current status of platinum-based antitumor drugs. *Chem. Rev.* **1999**, *99*, 2451−2466.

(9) Lokich, J. What is the "best" platinum: cisplatin, carboplatin, or oxaliplatin? *Cancer Invest.* **2001**, *19*, 756−760.

(10) Bruijnincx, P. C.; Sadler, P. J. Controlling platinum, ruthenium, and osmium reactivity for anticancer drug design. *Adv. Inorg. Chem.* **2009**, *61*, 1−62.

(11) Avan, A.; Postma, T. J.; Ceresa, C.; Avan, A.; Cavaletti, G.; Giovannetti, E.; Peters, G. J. Platinum-induced neurotoxicity and preventive strategies: past, present, and future. *Oncologist* **2015**, *20*, 411−432.

(12) Lenis-Rojas, O. A.; Roma-Rodrigues, C.; Fernandes, A. R.; Marques, F.; Perez-Fernandez, D.; Guerra-Varela, J.; Sanchez, L.; Vazquez-Garcia, D.; Lopez-Torres, M.; Fernandez, A.; Fernandez, J. J. Dinuclear RuII (bipy) 2 derivatives: Structural, biological, and in vivo zebrafish toxicity evaluation. *Inorg. Chem.* **2017**, *56*, 7127−7144.

(13) Brabec, V.; Nováková, O. DNA binding mode of ruthenium complexes and relationship to tumor cell toxicity. *Drug Resistance Updates* **2006**, *9*, 111−122.

(14) Pal, M.; Nandi, U.; Mukherjee, D. Detailed account on activation mechanisms of ruthenium coordination complexes and their role as antineoplastic agents. *Eur. J. Med. Chem.* **2018**, *150*, 419−445.

(15) Groessl, M.; Reisner, E.; Hartinger, C. G.; Eichinger, R.; Semenova, O.; Timerbaev, A. R.; Jakupec, M. A.; Arion, V. B.; Keppler, B. K. Structure−activity relationships for NAMI-A-type complexes (HL)[trans-RuCl4L (S-dmso) ruthenate (III)](L = imidazole, indazole, 1, 2, 4-triazole, 4-amino-1, 2, 4-triazole, and 1-methyl-1, 2, 4-triazole): Aquation, redox properties, protein binding, and antiproliferative activity. *J. Med. Chem.* **2007**, *50*, 2185−2193.

(16) Trondl, R.; Heffeter, P.; Kowol, C. R.; Jakupec, M. A.; Berger, W.; Keppler, B. K. NKP-1339, the first ruthenium-based anticancer drug on the edge to clinical application. *Chem. Sci.* **2014**, *5*, 2925−2932.

(17) Leijen, S.; Burgers, S. A.; Baas, P.; Pluim, D.; Tibben, M.; van Werkhoven, E.; Alessio, E.; Sava, G.; Beijnen, J. H.; Schellens, J. H. Phase I/II study with ruthenium compound NAMI-A and gemcitabine in patients with non-small cell lung cancer after first line therapy. *Invest. New Drugs* **2015**, *33*, 201−214.

(18) Gransbury, G. K.; Kappen, P.; Glover, C. J.; Hughes, J. N.; Levina, A.; Lay, P. A.; Musgrave, I. F.; Harris, H. H. Comparison of KP1019 and NAMI-A in tumour-mimetic environments. *Metallomics* **2016**, *8*, 762−773.

(19) Bergamo, A.; Pelillo, C.; Chambery, A.; Sava, G. Influence of components of tumour microenvironment on the response of HCT-116 colorectal cancer to the ruthenium-based drug NAMI-A. *J. Inorg. Biochem.* **2017**, *168*, 90−97.

(20) Li, G.; Sun, L.; Ji, L.; Chao, H. Ruthenium (ii) complexes with dppz: from molecular photoswitch to biological applications. *Dalton Trans.* **2016**, *45*, 13261−13276.

(21) Levina, A.; Mitra, A.; Lay, P. A. Recent developments in ruthenium anticancer drugs. *Metallomics* **2009**, *1*, 458−470.

(22) Mutua, G. K.; Bellam, R.; Jaganyi, D.; Mambanda, A. The role of N, N-chelate ligand on the reactivity of (η6-p-cymene) Ru (II) complexes: kinetics, DNA and protein interaction studies. *J. Coord. Chem.* **2019**, *72*, 2931−2956.

(23) Bellam, R.; Jaganyi, D.; Mambanda, A.; Robinson, R. Role of a 2,3-bis(pyridyl)pyrazinyl chelate bridging ligand in the reactivity of Ru (ii)−Pt (ii) dinuclear complexes on the substitution of chlorides by thiourea nucleophiles−a kinetic study. *New J. Chem.* **2018**, *42*, 12557−12569.

(24) van Boom, S. S.; Chen, B. W.; Teuben, J. M.; Reedijk, J. Platinum−thioether bonds can be reverted by guanine−N7 bonds in Pt (dien) 2+ model adducts. *Inor. Chem.* **1999**, *38*, 1450−1455.

(25) Rau, T.; Alsfasser, R.; Zahl, A.; van Eldik, R. Structural and kinetic studies on the formation of platinum (II) and palladium (II) complexes with L-cysteine-derived ligands. *Inorg. Chem.* **1998**, *37*, 4223−4230.

(26) Shoukry, A. A. Kinetics and mechanism for the substitution reactions of monoaquamonochloro-(piperazine) palladium (II) complex with L-methionine and thiourea in aqueous solution. *J. Chem. Sci.* **2013**, *125*, 643−651.

(27) Hochreuther, S.; van Eldik, R. Reactivity of a cytostatic active N,N-donor-containing dinuclear Pt (II) complex with biological relevant nucleophiles. *Inorg. Chem.* **2012**, *51*, 3025−3038.

(28) Summa, N.; Schiessl, W.; Puchta, R.; van Eikema Hommes, N.; van Eldik, R. Thermodynamic and kinetic studies on reactions of Pt (II) complexes with biologically relevant nucleophiles. *Inorg. Chem.* **2006**, *45*, 2948−2959.

(29) Zhu, S.; Matilla, A.; Tercero, J. M.; Vijayaragavan, V.; Walmsley, J. A. Binding of palladium (II) complexes to guanine, guanosine or guanosine 5′-monophosphate in aqueous solution: potentiometric and NMR studies. *Inorg. Chim. Acta* **2004**, *357*, 411−420.

(30) Soldatović, T.; Jovanović, S.; Bugarčić, Ž. D.; van Eldik, R. Substitution behaviour of novel dinuclear Pt (II) complexes with bio-relevant nucleophiles. *Dalton Trans.* **2012**, *41*, 876−884.

(31) Jovanović, S.; Petrović, B.; Čanović, D.; Bugarčić, Ž. D. Kinetics of the substitution reactions of some Pt (II) complexes with 5′-GMP and l-histidine. *Int. J. Chem. Kinet.* **2011**, *43*, 99−106.

(32) Loftus, L. M.; Olson, E. C.; Stewart, D. J.; Phillips, A. T.; Arumugam, K.; Cooper, T. M.; Haley, J. E.; Grusenmeyer, T. A. Zn Coordination and the Identity of the Halide Ancillary Ligand Dramatically Influence the Excited-State Dynamics and Bimolecular Reactions of 2, 3-Di (pyridin-2-yl) benzo [g] quinoxaline. *Inorg. Chem.* **2021**, *60*, 16570−16583.

(33) Soldatović, T.; Bugarčić, Ž. D. Study of the reactions between platinum (II) complexes and L-methionine in the presence and absence of 5′-GMP. *J. Inorg. Biochem.* **2005**, *99*, 1472−1479.

(34) Jovanović, S.; Obrenčević, K.; Bugarčić, Ž. D.; Popović, I.; Žakula, J.; Petrović, B. New bimetallic palladium (II) and platinum (II) complexes: studies of the nucleophilic substitution reactions, interactions with CT-DNA, bovine serum albumin and cytotoxic activity. *Dalton Trans.* **2016**, *45*, 12444−12457.

(35) Murray, S. G.; Hartley, F. R. Coordination chemistry of thioethers, selenoethers, and telluroethers in transition-metal complexes. *Chem. Rev.* **1981**, *81*, 365−414.

(36) Ćoćić, D.; Jovanović, S.; Radisavljević, S.; Korzekwa, J.; Scheurer, A.; Puchta, R.; Baskić, D.; Todorović, D.; Popović, S.; Matić, S.; Petrović, B. New monofunctional platinum (II) and palladium (II) complexes: Studies of the nucleophilic substitution reactions, DNA/BSA interaction, and cytotoxic activity. *J. Inorg. Biochem.* **2018**, *189*, 91−102.

(37) Omondi, R. O.; Bellam, R.; Ojwach, S. O.; Jaganyi, D.; Fatokun, A. A. Palladium (II) complexes of tridentate bis (benzazole) ligands: Structural, substitution kinetics, DNA interactions and cytotoxicity studies. *J. Inorg. Biochem.* **2020**, *210*, No. 111156.

(38) Bellam, R.; Anipindi, N. R.; Jaganyi, D. Effect of CTAB and SDS on base hydrolysis of iron (II)-sulphonated and unsulphonated phenyl-1, 2, 4-triazine complexes-A kinetic and mechanistic study. *J. Mol. Liq.* **2018**, *258*, 57−65.

(39) Pregosin, P. S. Platinum-195 nuclear magnetic resonance. *Coord. Chem. Rev.* **1987**, *44*, 247−291.

(40) Ferrari, E.; Grandi, R.; Lazzari, S.; Marverti, G.; Rossi, M. C.; Saladini, M. 1H, 13C, 195Pt NMR study on platinum (II) interaction with sulphur containing Amadori compounds. *Polyhedron* **2007**, *26*, 4045−4052.

(41) Still, B. M.; Kumar, P. A.; Aldrich-Wright, J. R.; Price, W. S. 195Pt NMR—Theory and application. *Chem. Soc. Rev.* **2007**, *36*, 665−686.

(42) Oehlsen, M. E.; Qu, Y.; Farrell, N. Reaction of polynuclear platinum antitumor compounds with reduced glutathione studied by multinuclear (1H, 1H− 15N gradient heteronuclear single-quantum coherence, and 195Pt) NMR spectroscopy. *Inorg. Chem.* **2003**, *42*, 5498−5506.

(43) Bellam, R.; Jaganyi, D.; Mambanda, A.; Robinson, R.; BalaKumaran, M. D. Seven membered chelate Pt (ii) complexes with 2, 3-di (2-pyridyl) quinoxaline ligands: studies of substitution kinetics by sulfur donor nucleophiles, interactions with CT-DNA, BSA and in vitro cytotoxicity activities. *RSC Adv.* **2019**, *9*, 31877−31894.

(44) Priqueler, J. R.; Butler, I. S.; Rochon, F. D. An overview of 195Pt nuclear magnetic resonance spectroscopy. *Appl. Spectrosc. Rev.* **2006**, *41*, 185−226.

(45) Ertürk, H.; Maigut, J.; Puchta, R.; van Eldik, R. Substitution behaviour of amine-bridged dinuclear Pt (II) complexes with bio-relevant nucleophiles. *Dalton Trans.* **2008**, *20*, 2759−2766.

(46) Ongoma, P. O.; Jaganyi, D. Mechanistic elucidation of linker and ancillary ligand substitution reactions in Pt (II) dinuclear complexes. *Dalton Trans.* **2013**, *42*, 2724−2734.

(47) Majid, M. H.; Mahdieh, G.; Leyla, M. Beyond a solvent: triple roles of dimethylformamide in organic chemistry. *RSC Adv.* **2018**, *8*, 27832−27862.

(48) Li, Z.; Michele, D. M.; Carmichael, I.; Sylwia, P. Electron-Induced Fragmentation of Methylated Formamides. *Int. J. Mass Spectrom.* **2016**, *410*, 36−46.

(49) Oehlsen, M. E.; Hegmans, A.; Qu, Y.; Farrell, N. A surprisingly stable macrochelate formed from the reaction of cis dinuclear platinum antitumor compounds with reduced glutathione. *Inorg. Chem.* **2005**, *44*, 3004−3006.

(50) Bierbach, U.; Roberts, J. D.; Farrell, N. Modification of platinum (II) antitumor complexes with sulfur ligands. 2. Reactivity and nucleotide binding properties of cationic complexes of the types [PtCl (diamine)(L)] NO3 and [{PtCl (diamine)} 2 (LL)](NO3) 2 (L = Monofunctional thiourea derivative; LL = Bifunctional thiourea derivative) in relation to their cytotoxicity. *Inorg. Chem.* **1998**, *37*, 717−723.

(51) Miller, S. K.; Marzilli, L. G. Interaction of platinum antitumor agents with guanine nucleosides and nucleotides. Platinum-195 and proton NMR spectroscopic characterization of compound III. *Inor. Chem.* **1985**, *24*, 2421−2425.

(52) Mansour, A. M.; Shehab, O. R. Lysozyme and DNA binding affinity of Pd (II) and Pt (II) complexes bearing charged N,N-pyridylbenzimidazole bidentate ligands. *Dalton Trans.* **2018**, *47*, 3459−3468.

(53) Komeda, S.; Moulaei, T.; Woods, K. K.; Chikuma, M.; Farrell, N. P.; Williams, L. D. A third mode of DNA binding: phosphate clamps by a polynuclear platinum complex. *J. Am. Chem. Soc.* **2006**, *128*, 16092−16103.

(54) Hotze, A. C.; Van der Geer, E. P.; Kooijman, H.; Spek, A. L.; Haasnoot, J. G.; Reedijk, J. Characterization by NMR Spectroscopy, X-ray Analysis and Cytotoxic Activity of the Ruthenium (II) Compounds [RuL3](PF6) 2 (L = 2-Phenylazopyridine or o-Tolylazopyridine) and [RuL′2L″](PF6) 2 (L′, L″= 2-Phenylazopyridine, 2, 2′-Bipyridine). *Eur. J. Inorg. Chem.* **2005**, *2005*, 2648−2657.

(55) Mitra, I.; Mukherjee, S.; Misini, B.; Das, P.; Dasgupta, S.; Linert, W.; Moi, S. C. Synthesis, biological evaluation, substitution behaviour and DFT study of Pd (II) complexes incorporating benzimidazole derivative. *New J. Chem.* **2018**, *42*, 2574−2589.

(56) Pyle, A. M.; Rehmann, J. P.; Meshoyrer, R.; Kumar, C. V.; Turro, N. J.; Barton, J. K. Mixed-ligand complexes of ruthenium (II): factors governing binding to DNA. *J. Am. Chem. Soc.* **1989**, *111*, 3051−3058.

(57) Cory, M.; McKee, D. D.; Kagan, J.; Henry, D. W.; Miller, J. A. Design, synthesis, and DNA binding properties of bifunctional intercalators. Comparison of polymethylene and diphenyl ether chains connecting phenanthridine. *J. Am. Chem. Soc.* **1985**, *107*, 2528−2536.

(58) Jayamani, A.; Bellam, R.; Gopu, G.; Ojwach, S. O.; Sengottuvelan, N. Copper (II) complexes of bidentate mixed ligands as artificial nucleases: Synthesis, crystal structure, characterization and evaluation of biological properties. *Polyhedron* **2018**, *156*, 138−149.

(59) Satyanarayana, S.; Dabrowiak, J. C.; Chaires, J. B. Tris (phenanthroline) ruthenium (II) enantiomer interactions with DNA: mode and specificity of binding. *Biochemistry* **1993**, *32*, 2573−2584.

(60) Dimiza, F.; Perdih, F.; Tangoulis, V.; Turel, I.; Kessissoglou, D. P.; Psomas, G. Interaction of copper (II) with the non-steroidal anti-inflammatory drugs naproxen and diclofenac: Synthesis, structure, DNA-and albumin-binding. *J. Inorg. Biochem.* **2011**, *105*, 476−489.

(61) Samari, F.; Hemmateenejad, B.; Shamsipur, M.; Rashidi, M.; Samouei, H. Affinity of two novel five-coordinated anticancer Pt (II) complexes to human and bovine serum albumins: a spectroscopic approach. *Inorg. Chem.* **2012**, *51*, 3454−3464.

(62) Yu, X.; Liu, R.; Yang, F.; Ji, D.; Li, X.; Chen, J.; Huang, H.; Yi, P. Study on the interaction between dihydromyricetin and bovine serum albumin by spectroscopic techniques. *J. Mol. Struct.* **2011**, *985*, 407−412.

(63) Rajendiran, V.; Karthik, R.; Palaniandavar, M.; Stoeckli-Evans, H.; Periasamy, V. S.; Akbarsha, M. A.; Srinag, B. S.; Krishnamurthy, H. Mixed-ligand copper (II)-phenolate complexes: effect of coligand on enhanced DNA and protein binding, DNA cleavage, and anticancer activity. *Inorg. Chem.* **2007**, *46*, 8208−8221.

(64) Cheng, Z. J.; Zhao, H. M.; Xu, Q. Y.; Liu, R. Investigation of the interaction between indigotin and two serum albumins by spectroscopic approaches. *J. Pharm. Anal.* **2013**, *3*, 257−269.

(65) Zehra, S.; Roisnel, T.; Arjmand, F. Enantiomeric amino acid schiff base copper (II) complexes as a new class of RNA-targeted metallo-intercalators: Single X-ray crystal structural details, comparative in vitro DNA/RNA binding profile, cleavage, and cytotoxicity. *ACS Omega* **2019**, *4*, 7691−7705.

(66) Maity, B.; Roy, M.; Saha, S.; Chakravarty, A. R. Photoinduced DNA and protein cleavage activity of ferrocene-conjugated ternary copper (II) complexes. *Organometallics* **2009**, *28*, 1495−1505.

(67) Petitpas, I.; Petersen, C. E.; Ha, C. E.; Bhattacharya, A. A.; Zunszain, P. A.; Ghuman, J.; Bhagavan, N. V.; Curry, S. Structural basis of albumin−thyroxine interactions and familial dysalbuminemic hyperthyroxinemia. *Proc. Natl. Acad. Sci. U. S. A.* **2003**, *100*, 440−6445.

(68) Ascenzi, P.; Di Masi, A.; Fanali, G.; Fasano, M. Heme-based catalytic properties of human serum albumin. *Cell Death Discovery* **2015**, *6*, No. e1895.

(69) Vijitphan, P.; Rukachaisirikul, V.; Muanprasat, C.; Iawsipo, P.; Panprasert, J.; Tadpetch, K. Unified synthesis and cytotoxic activity of

8-O-methylfusarubin and its analogues. *Org. Biomol. Chem.* **2019**, *17*, 7078−7087.

(70) Swaminathan, S.; Haribabu, J.; Kalagatur, N. K.; Konakanchi, R.; Balakrishnan, N.; Bhuvanesh, N.; Karvembu, R. Synthesis and anticancer activity of [RuCl2 (η6-arene)(aroylthiourea)] complexes—high activity against the human neuroblastoma (IMR-32) cancer cell line. *ACS Omega* **2019**, *4*, 6245−6256.

(71) Tokala, R.; Thatikonda, S.; Vanteddu, U. S.; Sana, S.; Godugu, C.; Shankaraiah, N. Design and Synthesis of DNA-Interactive β-Carboline−Oxindole Hybrids as Cytotoxic and Apoptosis-Inducing Agents. *Chem. Med. Chem.* **2018**, *13*, 1909−1922.

(72) Mandrekar, N.; Thakur, N. L. Significance of the zebrafish model in the discovery of bioactive molecules from nature. *Biotechnol. Lett.* **2009**, *31*, 171−179.

(73) MacRae, C. A.; Peterson, R. T. Zebrafish as tools for drug discovery. *Nat. Rev. Drug Discovery* **2015**, *14*, 721−731.

(74) Choi, J.; Im, G. J.; Chang, J.; Chae, S. W.; Lee, S. H.; Kwon, S. Y.; Chung, A. Y.; Park, H. C.; Jung, H. H. Protective effects of apocynin on cisplatin-induced ototoxicity in an auditory cell line and in zebrafish. *J. Appl. Toxicol.* **2013**, *33*, 125−133.

(75) Ma, L.; Lin, X.; Li, C.; Xu, Z.; Chan, C. Y.; Tse, M. K.; Shi, P.; Zhu, G. A cancer cell-selective and low-toxic bifunctional heterodinuclear Pt (IV)−Ru (II) anticancer prodrug. *Inorg. Chem.* **2018**, *57*, 2917−2924.

(76) Osterauer, R.; Haus, N.; Sures, B.; Köhler, H. R. Uptake of platinum by zebrafish (Danio rerio) and ramshorn snail (Marisa cornuarietis) and resulting effects on early embryogenesis. *Chemosphere* **2009**, *77*, 975−982.

(77) Živković, M. D.; Kljun, J.; Ilic-Tomic, T.; Pavic, A.; Veselinović, A.; Manojlović, D. D.; Nikodinovic-Runic, J.; Turel, I. A new class of platinum (II) complexes with the phosphine ligand pta which show potent anticancer activity. *Inorg. Chem. Front.* **2018**, *5*, 39−53.

(78) Hirose, Y.; Simon, J. A.; Ou, H. C. Hair cell toxicity in anti-cancer drugs: evaluating an anti-cancer drug library for independent and synergistic toxic effects on hair cells using the zebrafish lateral line. *J. Assoc. Res. Otolaryngol* **2011**, *12*, 719−728.

(79) Sirajuddin, M.; Ali, S.; Badshah, A. Drug−DNA interactions and their study by UV−Visible, fluorescence spectroscopies and cyclic voltametry. *J. Photochem. Photobiol., B* **2013**, *124*, 1−19.

(80) Novakova, O.; Chen, H.; Vrana, O.; Rodger, A.; Sadler, P. J.; Brabec, V. DNA interactions of monofunctional organometallic ruthenium (II) antitumor complexes in cell-free media. *Biochemistry* **2003**, *42*, 11544−11554.

(81) Chichak, K.; Jacquemard, U.; Branda, N. R. The construction of (salophen) ruthenium (II) assemblies using axial coordination. *Eur. J. Inorg. Chem.* **2002**, *2002*, 357−368.

(82) Meyer-Almes, F. J.; Porschke, D. Mechanism of intercalation into the DNA double helix by ethidium. *Biochemistry* **1993**, *32*, 4246−4253.

(83) Ramachandran, E.; Senthil Raja, D.; Rath, N. P.; Natarajan, K. Role of substitution at terminal nitrogen of 2-oxo-1, 2-dihydroquinoline-3-carbaldehyde thiosemicarbazones on the coordination behavior and structure and biological properties of their palladium (II) complexes. *Inorg. Chem.* **2013**, *52*, 1504−1514.

(84) Parker, C. A.; Rees, W. T. Fluorescence spectrometry. A review. *Analyst* **1962**, *87*, 83−111.

(85) Puchalski, M. M.; Morra, M. J.; Von Wandruszka, R. Assessment of inner filter effect corrections in fluorimetry. *Fresenius' J. Anal. Chem.* **1991**, *340*, 341−344.

(86) Laemmli, U. K. Cleavage of structural proteins during the assembly of the head of bacteriophage T4. *Nature* **1970**, *227*, 680−685.

(87) Westerfield, M. *The zebrafish book: a guide for the laboratory use of zebrafish*, 2000, http://zfin.org/zf_info/zfbook/zfbk.html.

(88) Bailey, M.; Williams, N. A.; Wilson, A. D.; Stokes, C. R. PROBIT: weighted probit regression analysis for estimation of biological activity. *J. Immunol. Methods* **1992**, *153*, 261.

(89) Abbott, W. S. A method of computing the effectiveness of an insecticide. *J. Econ. Entomol.* **1925**, *18*, 265−267.